Journal of Pharmaceutical Analysis 15 (2025) 101077

Contents lists available at ScienceDirect

Journal of Pharmaceutical Analysis

journal homepage: www.elsevier.com/locate/jpa

Original article

Exploring the impact of the liver-intestine-brain axis on brain function in non-alcoholic fatty liver disease

Jingting Zhang [a, b], Keyan Chen [c, *], Fu Chen [d, **]

[a] College of Management, Liaoning Economy Vocational and Technical College, Shenyang, 110122, China
[b] Department of Nutrition and Food Hygiene, School of Public Health, China Medical University, Shenyang, 110122, China
[c] Department of Laboratory Animal Science, China Medical University, Shenyang, 110122, China
[d] Department of General Surgery, Fourth Affiliated Hospital of China Medical University, Shenyang, 110032, China

ARTICLE INFO

Article history:
Received 24 January 2024
Received in revised form
12 August 2024
Accepted 16 August 2024
Available online 19 August 2024

Keywords:
Non-alcoholic fatty liver disease
Liver-intestine-brain axis
Microbiota shifts
Deoxycholic acid
Microglial cells
JAK2/STAT3 signaling
Brain dysfunction

ABSTRACT

This study investigates the molecular complexities of non-alcoholic fatty liver disease (NAFLD)-induced brain dysfunction, with a focus on the liver-intestine-brain axis and potential therapeutic interventions. The main objectives include understanding critical microbiota shifts in NAFLD, exploring altered metabolites, and identifying key regulatory molecules influencing brain function. The methods employed encompassed 16S ribosomal RNA (rRNA) sequencing to scrutinize stool microbiota in NAFLD patients and healthy individuals, non-targeted metabolomics using LC-MS to uncover elevated levels of deoxycholic acid (DCA) in NAFLD mice, and single-cell RNA sequencing (scRNA-seq) to pinpoint the pivotal gene Hpgd in microglial cells and its downstream Janus kinase 2/signal transducer and activator of transcription 3 (JAK2/STAT3) signaling pathway. Behavioral changes and brain function were assessed in NAFLD mice with and without Fecal microbiota transplantation (FMT) treatment, utilizing various assays and analyses. The results revealed significant differences in microbiota composition, with increased levels of *Bacteroides* in NAFLD patients. Additionally, elevated DCA levels were observed in NAFLD mice, and FMT treatment demonstrated efficacy in ameliorating liver function and brain dysfunction. Hpgd inhibition by DCA activated the JAK2/STAT3 pathway in microglial cells, leading to inflammatory activation, inhibition of mitochondrial autophagy, induction of neuronal apoptosis, and reduction in neuronal action potentials. This study elucidates the intricate molecular mechanisms underlying the liver-gut-brain axis in NAFLD, and the identification of increased DCA and the impact of JAK2/STAT3 signaling on microglial cells highlight potential therapeutic targets for addressing NAFLD-induced brain dysfunction.

1. Introduction

Non-alcoholic fatty liver disease (NAFLD) has emerged as the predominant chronic liver disease globally, with a continuously growing prevalence that poses a substantial threat to public health [1,2]. NAFLD is not only linked to liver diseases but also closely associated with a range of systemic conditions, including cardiovascular diseases, renal diseases, and metabolic syndrome [3,4]. Recent research has increasingly shown that NAFLD may be linked to cognitive impairments [5,6]. Specifically, certain patients may present with clinical symptoms associated with the central nervous system, such as impairments in learning and memory and emotional fluctuations [7]. However, the precise connection between NAFLD and cognitive dysfunction and its underlying mechanisms remains uncertain.

In the meantime, the gut microbiota plays a pivotal role in developing NAFLD [8,9]. It is widely recognized that the gut is the area of the human body with the highest concentration of microbiota, and how it interacts with the host influences individuals' health and disease status [10]. Recent research has revealed a reciprocal relationship between the liver and the intestine, commonly known as the “liver-gut axis” [11]. Dysbiosis of the gut microbiota in patients with NAFLD could potentially impact liver health by increasing intestinal permeability, leading to the entry of endotoxins into the liver and subsequent initiation of inflammatory responses [12]. However, the impact of such dysfunction on brain

---

* Corresponding author.
** Corresponding author.
E-mail addresses: kychen@cmu.edu.cn (K. Chen), 20161047@cmu.edu.cn (F. Chen).

Peer review under responsibility of Xi'an Jiaotong University.

https://doi.org/10.1016/j.jpha.2024.101077

function, specifically on the signaling pathways and molecular mechanisms, has not been fully understood.

To delve deeper into this, the study utilized cutting-edge biotechnological techniques, including 16S ribosomal RNA (rRNA) sequencing and single-cell transcriptome sequencing [13]. These techniques enable the in-depth analysis of the composition and function of gut microbiota, identifying key microorganisms associated with NAFLD [14]. In addition, we performed a thorough analysis of fecal metabolites in mice with NAFLD using untargeted metabolomics combined with liquid chromatography-mass spectrometry (LC-MS) [12]. These methods offer a comprehensive perspective, spanning from microorganisms to metabolites and extending to signal transduction pathways, to investigate the potential influence of NAFLD on brain function.

Furthermore, we have extensively researched the correlation between the principal metabolite, deoxycholic acid (DCA), and cognitive impairment in individuals with NAFLD. Bacteria produce DCA in the intestinal tract; it could then enter the liver, ultimately impacting other organs, such as the brain. This study uncovers how DCA induces brain dysfunction by modulating specific signaling pathways, notably the hydroxyprostaglandin dehydrogenase (HPGD)/Janus kinase 2 (JAK2)/signal transducer and activator of transcription 3 (STAT3) pathway. It offers a novel perspective that enhances our comprehension of the influence of NAFLD on brain function, along with potential strategies for treatment.

2. Materials and methods

2.1. Ethics statement

This study was conducted in strict accordance with the ethical guidelines for animal research and was approved by the Institutional Animal Care and Use Committee of China Medical University, China (Approval number: CMU2022278).

2.2. 16S rRNA sequencing data acquisition

Relevant projects were retrieved using the EMBL-EBI database (https://www.ebi.ac.uk/ena/browser/search) by searching for the keyword ‘non-alcoholic fatty liver disease’. The phenotype information of all samples from the project with the BioProject number PRJNA860335 was downloaded. Subsequently, the 16S rRNA sequencing data of the samples was retrieved from the NCBI Sequence Read Archive (SRA) database, which can be accessed at https://www.ncbi.nlm.nih.gov/sra/. The project included six stool samples from patients with NAFLD and six from normal control subjects.

2.3. Microbial relative abundance analysis

The samples were evaluated using multiQC and KneadData. MultiQC was employed for sequencing quality control, while KneadData was utilized for the removal of host and contaminant sequences. GraPhlAn was used to generate a microbial species tree with annotations for differential analysis, providing the relative abundance of microbial classifications. To assess the species complexity and diversity within the samples, alpha diversity analysis was conducted using the inverse Simpson index, while beta diversity analysis was carried out through principal coordinate analysis (PCoA).

The Wilcoxon rank-sum test and Welch's *t*-test were employed to compare bacterial abundance and diversity. The R software package edgeR was utilized to calculate inter-group abundance differences and to create volcano plots and Manhattan plots. Differential abundance bar graphs were generated through the linear discriminant analysis effect size (LEfSe) analysis, with a linear discriminant analysis (LDA) score threshold set at 2.0. The LDA score reflects the impact of significantly different species between groups, with higher scores indicating greater differentiation in characteristics between the two groups.

2.4. Microbial functional composition

The FAPROTAX dataset is an artificially constructed database of prokaryotic taxonomic groups used to predict microbial communities' primary ecological functions. QIIME data are transformed using a combination of R packages, followed by a community phylogenetic investigation using phylogenetic investigation of communities by reconstruction of unobserved states (PICRUSt). We used the Kyoto Encyclopedia of Genes and Genomes (KEGG) to predict the metagenomic pathway for each primer set.

Statistical analysis and visualization were conducted on the unstratified results using the STAMP software (v2.1.3). Welch's *t*-test is commonly employed to compare differences in the composition of functional groups.

2.5. Mouse model generation

Wild-type male BALB/c mice, aged 4 weeks and weighing 16–20 g, were sourced from our Experimental Animal Research Center. Two dietary treatments were carried out on littermate mice: a normal diet (ND) and a high-fat, high-sucrose diet (HFD; 16.9% fat, 1.3% cholesterol, 21.1% crude protein, and 46.5% carbohydrates; XT108C, Cyagen, Suzhou, China). Feeding mice with HFD for 8 week could induce NAFLD, whereas prolonged feeding for 16 week could impair brain function.

The mice were euthanized by cervical dislocation using isoflurane (R510-22-10, Rayward, Shenzhen, China). Blood samples were collected to assess hematological and biochemical parameters. Liver or brain tissue was obtained for histological analysis.

Fecal microbiota transplantation (FMT) involves collecting feces from mice on an ND and combining them into a pooled sample. This sample is then diluted using cold phosphate-buffered saline (PBS) at a ratio of 100 mg feces per 1 mL of buffer solution. Afterward, the sample was mixed thoroughly for 10 min until it achieved a paste-like consistency. It should then be vortexed for 1 min and centrifuged at 800 *g* for 5 min. The supernatant was collected, divided, and stored in an 80% glycerol-PBS solution at −20 °C until transplantation.

A daily oral gavage of 1 mL antibiotic mixture was administered to reduce the bacterial load in recipient mice. The mixture included vancomycin (50 mg/kg; 1404-93-9, Sigma-Aldrich, St. Louis, MO, USA), neomycin (100 mg/kg; 1405-10-3, Sigma-Aldrich, St. Louis, MO, USA), metronidazole (100 mg/kg; 13182-89-3, Sigma-Aldrich, St. Louis, MO, USA), and amphotericin B (1 mg/kg; 1397-89-3, Sigma-Aldrich, St. Louis, MO, USA). This administration continued for 7 consecutive days. Additionally, they supplemented their drinking water with ampicillin (1 g/L; A5354, Sigma-Aldrich, St. Louis, MO, USA).

Following antibiotic treatment, the recipient mice received 1 mL of donor fecal microbiota supernatant by gavage every other day until they were euthanized [15].

Model groups included the ND group (mice fed a normal diet) and the HFD group (mice fed a high-fat diet (HFD)). The FMT treatment groups consisted of the Normal group (mice fed a normal diet), the NAFLD-saline group (NAFLD mice fed with physiological saline as a control for FMT), and the NAFLD-FMT group (NAFLD mice undergoing FMT).

2.6. Liver function test

Peripheral blood was collected from mice, and serum alanine aminotransferase (ALT), aspartate aminotransferase (AST), triglycerides (TAG), low-density lipoprotein (LDL), and high-density lipoprotein (HDL) were measured using the Vitros 5.1FS automated biochemical analyzer (Ortho Clinical Diagnostics, Raritan, NJ, USA) [16].

2.7. Pathology histology staining

Hematoxylin and eosin (H&E) staining was performed by obtaining liver tissue samples from mice that were undergoing fixation. After sectioning, the wax blocks were treated with xylene to remove the wax, followed by dehydration in sequential concentrations of ethanol − 100% ethanol (64-17-5, Sigma-Aldrich, St. Louis, MO, USA), 95% ethanol, and 70% ethanol. Finally, embedding or washing with water was done. For staining, the prepared slices were placed in the Sudan III staining solution (H8070, Solarbio, Beijing, China). Typically, this is done at room temperature for 5–10 min. Next, the slides were washed with distilled water, dehydrated using 95% ethanol, and immersed in the Yihong staining solution (G1100, Solarbio, Beijing, China) for 5–10 min. After the routine dehydration process, the slides became transparent and ready to be sealed.

2.8. Open field test (OFT)

The mice was placed in an open-air arena measuring 100 cm × 100 cm × 45 cm. They should then be given 6 min to freely explore. The open area is divided into 16 square fields, with four middle fields designated as the central zone. The distance covered and the time to enter and exit the central area were determined [17].

2.9. Morris water maze (MWM) test

The pool is black circular in shape, with a diameter of 150 cm and a height of 50 cm. It has a temperature of 23 ± 1 °C and a water depth of 45 cm. The pool is divided into four equal quadrants by four equidistant points on the wall. The transparent escape platform is submerged approximately 1.5–2.0 cm below the water surface in quadrant IV's center.

During the five-day trial phase of consecutive collections, mice were gently positioned facing the maze wall at one of the four predetermined starting positions. The time to locate the hidden platform (escape latency) was recorded. The mice were directed toward the platform and remained there for 10 s. If they cannot locate the platform, the maximum scoring time is 120 s. It is recommended to perform four experiments daily, ensuring that each experiment does not exceed 2 min. There was a 15-s interval between each experiment. On the sixth day, probe trials were conducted by placing each mouse in a different starting position to swim in the pool without a platform for 120 s. This study aims to document and analyze the duration and frequency of the participant's engagement in the previous quadrant on the platform.

2.10. Western blot

Total proteins were extracted from cells and tissues. Cultured cells and tissues were digested and collected using trypsin (T4799-5G, Sigma-Aldrich, St. Louis, MO, USA). Cell lysis was conducted using an enhanced radioimmunoprecipitation assay (RIPA) lysis buffer containing a protease inhibitor cocktail (AR0108, Wuhan Boditech Biotechnology Co., Ltd., Wuhan, China). Protein concentration was determined with the BCA protein quantification kit (AR1189, Wuhan Boditech Biotechnology Co., Ltd., Wuhan, China).

The mitochondrial isolation kit (LM-319921-1, LMal Bio, Shanghai, China) was utilized to isolate mitochondria from cells. In brief, the cells were collected, washed with pre-chilled PBS, and resuspended in a ten-fold volume of pre-chilled mitochondrial lysis buffer. The sample was placed on ice and homogenized using a homogenizer, mortar, and pestle. The samples were centrifuged at 4 °C for 5 min at 600 *g* to remove nuclei and intact fragments of the nuclear envelope. The sediment was removed and the supernatant was transferred to a new centrifuge tube. The supernatant was centrifuged at 12,000 *g* for 10 min at 4 °C. Precipitation is the complete mitochondria. To the residue, 200 μL of C5032-C and 2 μL of 100 mM Phenylmethylsulfonyl fluoride (PMSF) were added. Next, the mixture was subjected to ultrasound treatment using an ice bath at 20% power (200 W) for 3 s with 10 s intervals, and this process was repeated 30 times. The concentration of mitochondrial proteins was determined by employing the bicinchoninic acid assay (BCA) protein quantification kit.

The proteins were first separated using sodium dodecyl sulfate-polyacrylamide gel electrophoresis (SDS-PAGE) and transferred onto a polyvinylidene fluoride (PVDF) membrane. For 1 h, the membrane was incubated at room temperature with 5% bovine serum albumin (BSA; 9048-46-8, Sigma-Aldrich, St. Louis, MO, USA). Afterward, the diluted primary antibody (Table S1) was added, and the membrane was incubated overnight at 4 °C. The membrane was washed three times with phosphate-buffered saline with Tween® 20 (PBST) for 5 min each time, then incubated at room temperature for 1 h with either the anti-mouse-horseradish peroxidase (HRP) secondary antibody (7076, 1/5000, CST, Danvers, MA, USA) or the anti-rabbit-HRP secondary antibody (7074, 1/5000, CST, Danvers, MA, USA). The membrane was then washed thrice with PBST for 5 min each time. PBST was removed, and an appropriate amount of electrochemiluminescence (ECL) working solution (Omt-01, Beijing Omni-Jade Pharmaceutical Technology Co., Ltd., Beijing, China) was added. The mixture was incubated at room temperature for 1 min. The excess ECL reagent was then removed, and the sample was sealed with plastic wrap and placed in a dark box. After 5–10 min of exposure, the development and fixation process was initiated. The bands in Western blot images were quantified using ImageJ software. Tubulin was used as the internal reference for grayscale quantification.

2.11. LC-MS

Fecal samples were collected from mice with HFD-induced NAFLD and normal mice after 16 week. Next, 300 μL of each sample was transferred to a 1.5 mL polypropylene tube. Next, the samples were mixed with 900 μL of 80% methanol (CAS No. 67-56-1, Sigma-Aldrich, St. Louis, MO, USA) and 0.1% formic acid (CAS No. 64-18-6, Sigma-Aldrich, St. Louis, MO, USA), followed by vortexing for 2 min and centrifugation at 12,000 *g* for 10 min. The clear upper liquid was transferred to the small vial of the auto-sampler.

We analyzed fecal metabolomics using the LC20 ultra-high performance liquid chromatography system (Shimadzu, Kyoto, Japan) with the Triple TOF-6600 mass spectrometer (AB Sciex, Framingham, MA, USA). For the chromatographic analysis, Waters ACQUITY UPLC HSS T3 C_{18} chromatographic column (Waters corporation, Milford, MA, USA) with dimensions of 100 mm × 2.1 mm and a particle size of 1.8 μm was recommended. The column was kept at a temperature of 40 °C, and elution was performed with a flow rate of 0.4 mL/min. The mobile phase comprised an aqueous acetonitrile solution (75-05-8, Sigma-Aldrich, St. Louis, MO, USA) containing 0.1% formic acid. The gradient elution program for mobile phase B was 5% from 0 to 11.0 min, 90% from 11.0 to 12.0 min, and 5% from 12.1 to 14 min. The shower gel was introduced directly into the mass spectrometer without undergoing fragmentation.

The conditions employed for positive/negative ion mode MS are as follows: ionization voltage at 5,500 V, capillary temperature at 550 °C, nebulizer gas flow rate at 50 psi, and auxiliary heating gas flow rate at 60 psi. The preprocessed data was analyzed using orthogonal partial least squares-discriminant analysis (OPLS-DA) and a permutation test with 100 permutations to prevent overfitting. Metabolites with variable importance in projection (VIP) scores greater than 1 and *P*-values less than 0.05 in the OPLS-DA model were identified as differential metabolites (DMs). Furthermore, the final differential metabolites were selected based on the univariate analysis, which included metabolites with fold changes greater than or equal to 2, fold changes less than or equal to 0.5, and *P*-values less than 0.05 in Student's *t*-test. MetaboAnalyst (Version 5.0) identified pertinent metabolic pathways.

2.12. Gas chromatography-MS (GC-MS)

After FMT, the serum from mice was collected. Then, 10 μL of ultrapure water was added for every 1 mL of serum. The mixture was thoroughly shaken and allowed to stand for 30 min. Subsequently, it was centrifuged at 4 °C and 12,000 rpm for 20 min. The supernatant was aspirated and filtered through a 0.22 μm hydrophilic membrane. Finally, the filtered sample was transferred to the desired gas phase bottle. The samples were treated with methanol and sulfuric acid under heating conditions to convert the carboxyl groups in bile acids to methyl esters. To enhance volatility, alkylations of hydroxyl groups were carried out using trimethylsilyl (TMS) reagent (1873-77-4, Xi'an Kaixin Biotechnology Co., Ltd., Xi'an, China). Following the derivatization reaction, the samples were washed and concentrated with n-hexane (CAS No. 110-54-3, Sigma-Aldrich, St. Louis, MO, USA).

The DB-WAX 30M chromatographic column (I.D. 0.32 mm, 5 μm; Agilent, Santa Clara, CA, USA) was employed, with the injection port and detector temperatures set at 250 °C each. The temperature program used in this study was as follows: initially, the temperature was maintained at 50 °C for 3 min. Subsequently, the temperature was increased at 6 °C per min until it reached 120 °C. After reaching 120 °C, it was maintained at that temperature for 0.5 min. Then, the temperature was increased at the same rate to attain 220 °C and maintained for 5 min. The flow rate of nitrogen was 3 mL/min, the flow rate of hydrogen was 47 mL/min, the flow rate of air was 400 mL/min, and the splitting ratio is 1:3. The sample volume was 1.0 μL. External standards was used for quantification. The content of each fatty acid in the sample was determined by calculating the ratio of the standard sample's peak area to the sample's peak area.

2.13. Electron microscope analysis of hippocampal structure

We collected mouse hippocampi for analysis using transmission electron microscopy (TEM). The hippocampus was dissected and treated with a cold fixative solution containing 2.5% glutaraldehyde (pH 7.2; CAS No. 111-30-8, Sigma-Aldrich, St. Louis, MO, USA) at 4 °C for 4 h. Subsequently, we performed three washes with PBS (0.1 M, pH 7.2). The specimens were subsequently fixed in a 1% osmium tetroxide solution (dissolved in 0.2 M PBS, pH 7.2; product number 20816-12-0, Predecessor Chemical Technology, Wuhan, China) at 4 °C for 1 h. It was followed by three washes using PBS (0.1 M, pH 7.2).

Subsequently, the specimen was dehydrated using a sequential immersion approach with ethanol solutions of varying concentrations (30%, 50%, 70%, 80%, 90%, and 100%) for 15−20 min per solution. Afterward, it was incubated in acetone (CAS No. 67-64-1, Sigma-Aldrich, St. Louis, MO, USA) for 20 min. The material was soaked in a 1:1 mixture of acetone and resin at 25 °C for 1 h, then transferred to an overnight 1:3 mixture of acetone and resin.

Finally, the ultra-thin slices were placed into embedding blocks away from the edge areas. The samples were stained with uranyl acetate (U25690, Shanghai Jizhi Biochemical Technology Co., Ltd., Shanghai, China) and lead citrate (CAS No. 512-26-5, Macklin, Shanghai, China) for 15 min. They were then observed using a JEM-1230 TEM (JEOL, Tokyo, Japan) operated at 80 kV and captured with a BioScan camera (Veleta, EMSIS GmbH, Münster, Germany) equipped with a side insertion [18].

2.14. Immunofluorescence and terminal deoxynucleotidyl transferase dUTP nick end labeling (TUNEL) staining

Initially, cells or tissues were washed with cold PBS, then fixated using 4% paraformaldehyde (P885233, Macklin, Shanghai, China) for 15−30 min. Next, the sample was treated with a 0.1% Triton solution (L885651, Macklin, Shanghai, China) for 15 min. Following two additional washes with PBS, the samples were then incubated in PBS supplemented with 15% fetal bovine serum (FBS) at a temperature of 5 °C for 4 min. To stain neurons (NeuN), we utilized the NeuN antibody (1:100; PA5-78499, Thermo Fisher, Waltham, MA, USA). For microglia staining (ionized calcium-binding adapter molecule 1 (Iba-1)), the Iba-1 antibody (1:100; MA5-27726, Thermo Fisher, Waltham, MA, USA) was employed. microtubule-associated protein 1 light chain 3 staining (LC3) staining was accomplished using the LC3 antibody (1:100; PA1-46286, Thermo Fisher, Waltham, MA, USA). The dye was applied to cells or tissues, which were then covered and incubated overnight at 4 °C.

Following three washes with TBST (1% Tween-20 in tris-buffered saline (TBS)), the cells were incubated with the appropriate secondary antibody for 2 h. Subsequently, the cell nuclei were stained with 4′,6-diamidino-2-phenylindole (DAPI; D1306, Thermo Fisher, Waltham, MA, USA), and their visualization was achieved through a fluorescence microscope (Zeiss Observer Z1, Carl Zeiss AG, Oberkochen, Germany). The desired image region was chosen and ImageJ software was utilized to measure fluorescence intensity and process the image.

For p62 staining (1:100; MA5-27800, Thermo Fisher, Waltham, MA, USA), the samples were incubated overnight at 4 °C. After incubation, the samples were washed with PBS to remove any unbound primary antibody or dye. Subsequently, the cells or tissues were treated with the translocase of outer mitochondrial membrane 20 (Tomm20) antibody (1:100; PA5-110506, Thermo Fisher, Waltham, MA, USA) for a second time, followed by an overnight incubation at 4 °C. Following three washes with TBST (1% Tween-20 in PBS), the cells were incubated with the appropriate secondary antibody for the respective species at room temperature for 2 h. Subsequently, the cell nuclei were stained with DAPI (D1306, Thermo Fisher, Waltham, MA, USA), and their visualization was achieved through a fluorescence microscope (Zeiss Observer Z1, Carl Zeiss AG, Oberkochen, Germany). The desired image region was chosen and utilize ImageJ software was utilized to measure fluorescence intensity and process the image.

Following the manufacturer's instructions, TUNEL staining was performed on brain sections using the TUNEL Cell Apoptosis Detection Kit (C1086, Beyotime, Shanghai, China). In summary, proteinase K (39450-01-6, Sigma-Aldrich, St. Louis, MO, USA) was added at 20 μg/mL to the slices without deoxyribonuclease (DNase). Following three washes with PBS, the samples were treated with a 50 mL TUNEL detection solution and then incubated in the dark at 37 °C for 60 min. The images were observed and analyzed using a Zeiss Observer Z1 fluorescence microscope (Carl Zeiss AG, Oberkochen, Germany) and ImageJ software.

2.15. Real-time quantitative reverse transcription polymerase chain reaction (RT-qPCR)

Cellular or tissue lysis was performed using the Trizol reagent (10296010, Invitrogen, Thermo Fisher, USA), extracting total cellular RNA. RNA quality and concentration were assessed using ultraviolet–visible spectrophotometry (ND-1000, Nanodrop, Thermo Fisher, Waltham, MA, USA). Reverse transcription was carried out using the PrimeScript™ RT-qPCR Kit (RR086A, TaKaRa, Mountain View, CA, USA). RT-qPCR was performed using SYBR Premix Ex TaqTM (DRR820A, TaKaRa, Mountain View, CA, USA) on a LightCycler 480 System (Roche Diagnostics, Pleasanton, CA, USA). The internal reference for messenger RNA (mRNA) was assessed using Tubulin as a reference gene. The primers utilized for amplification were designed and supplied by Shanghai Universal Biotech Co., Ltd. (Shanghai, China). The primer sequences are shown in Table S2. The term $2^{-\Delta\Delta Ct}$ was used to quantify the relative change in target gene expression between the experimental and control groups. It was calculated through the formula: $\Delta\Delta Ct = \Delta Ct$ experimental group $-$ ΔCt control group. ΔCt refers to the difference between the Ct values of the target gene and the reference gene.

2.16. Single-cell transcriptome sequencing (scRNA-seq)

The hippocampal tissue from the mice above was collected and processed into a single-cell suspension utilizing trypsin (9002-07-7, Sigma-Aldrich, St. Louis, MO, USA), and individual cells were subsequently captured using the C1 single-cell auto-preparation system (Fluidigm, Inc., South San Francisco, CA, USA). Once the single cells were captured, they lysed within the chip to extract mRNA. Subsequently, reverse transcription was conducted to produce complementary DNA (cDNA). The cDNA, which has undergone post-digestion and reverse transcription, was pre-amplified on a microfluidic chip in preparation for sequencing. The amplified cDNA was used for library construction, and single-cell sequencing was conducted on the HiSeq 4000 Illumina platform (Illumina, Inc., San Diego, CA, USA). The sequencing parameters included paired-end sequencing with a read length of 2 × 75 bp, and approximately 20,000 reads were obtained per cell.

The data was analyzed using the “Seurat” package in the R software. Data quality control was performed using 200 < nFeature_RNA < 5000 percent criteria.mt < 20. Subsequently, highly variable genes with the top 2000 variances were selected for further analysis. To decrease the dimensionality of scRNA-seq datasets, we utilized principal component analysis (PCA) on the data, considering the top 2000 genes with high variability based on variance.

The downstream analysis was conducted by selecting the initial 20 principal components (PCs) utilizing the Elbowplot function within the Seurat package. To identify major cell subgroups, the FindClusters function provided by Seurat was used, with the resolution set to the default value (res = 1). Subsequently, the t-distributed Stochastic neighborhood embedding (*t*-SNE) algorithm was utilized to reduce the nonlinear dimension of scRNA-seq sequencing data. Marker genes of different cell subpopulations were screened using the Seurat package, and cell annotation was performed using the “SingleR” package.

We utilized the R package called “CellChat” for analyzing cell communication and the package “Monocle2” for performing cell trajectory analysis. The differential expression of genes (DEGs) in scRNA-Seq datasets could be screened using the “Limma” package in the R software. The DEGs between different samples were filtered out.

2.17. Cell culture

The BV2 mouse microglial cell line (SNL-15, Sean Biotech, Wuhan, China) and the HT22 mouse hippocampal neuron cell line (SNL-202, Sean Biotech, Wuhan, China) were grown in Dulbecco's modified Eagle medium (DMEM; 11965092, Gibco, Grand Island, NY, USA) supplemented with 10% FBS (TMS-016, Sigma Aldrich, St. Louis, MO, USA), 10 μg/mL streptomycin (85886, Sigma Aldrich, St. Louis, MO, USA), and 100 U/mL penicillin (9073-60-3, Sigma Aldrich, St. Louis, MO, USA). The cells were cultured in a Heracell™ Vios 160i CR CO_2 Incubator (model 51033770, Thermo Scientific™, Waltham, MA, USA) at 37 °C and with 5% CO_2 in a humidified environment. Once the cells reached 80%–90% confluence, it was necessary to perform a passaging culture.

Microglial cell activation was inducted by lipopolysaccharide (LPS): BV2 cells were treated with LPS (100 ng/mL) (L5293, Sigma Aldrich, St. Louis, MO, USA) to activate microglial cells. The cells were then stimulated for 24 h in preparation for subsequent experiments. BV2 cells were incubated with dichloroacetate (DCA; CAS No. 83-44-3, Sigma Aldrich, St. Louis, USA) at varying concentrations (0, 100, 200, 400, 600, or 800 μM).

The pCAGGs-GFP plasmid (HG-VPH1278, Equl, Shanghai, China) expressing green fluorescent protein (GFP) was transfected into HT22 cells using Lipofectamine 2000 (11668030, Thermo Fisher, Waltham, MA, USA). After 24 h, co-culture with BV2 cells of different genotypes was performed.

To investigate the influence of microglia on neurons, the culture supernatant was collected from BV2 cells after 24 h of LPS stimulation. Subsequently, the supernatant was mixed with a regular culture medium in a 1:1 ratio. The resulting mixture was added to HT22 cells and incubated for 24 h before further experimental analysis.

The cell groups were as follows: the NC-UP group (overexpressing control plasmid in BV2 cells), the Hpgd-UP group (overexpressing *Hpgd* in BV2 cells), the STAT3-UP group (overexpressing *Stat3* in BV2 cells), the PBS group (adding PBS to BV2 cells as a DCA control), the DCA group (adding DCA to BV2 cells), the PBS-NC-UP group (adding PBS to BV2 cells and transfecting with control plasmid), the DCA-NC-UP group (adding DCA to BV2 cells and transfecting with control plasmid), the DCA-Hpgd-UP group (adding DCA to BV2 cells and transfecting with *Hpgd* overexpression plasmid), and the Hpgd + STAT3-UP group (overexpressing both *Hpgd* and *Stat3* in BV2 cells).

2.18. Lactate dehydrogenase (LDH) release test

After treatment with DCA, the culture supernatant was collected. The LDH levels in the supernatant were measured using the LDH cytotoxicity assay kit (ab102526, Abcam, Cambridge, UK) following the manufacturer's instructions. Briefly, prior to adding the working solution, the maximum LDH release control was added with 20 μL of 10 × lysis solution for 45 min. Subsequently, 120 μL of the supernatant was transferred to a new 96-well plate, and 60 μL of the working solution was added to each well, followed by incubation at room temperature in the dark for 25 min. The absorbance at 490 nm was then measured using a microplate reader (HBS-1096C, Detie, Nanjing, China).

2.19. Lentivirus

The plasmid pCMV6-AC-GFP (LM-2069, LMAI Bio, Shanghai, China), which induces overexpression of the genes *Hpgd* and *Stat3*, was constructed by Geneworks Biotech Company (Shanghai, China). Hpgd-UP and STAT3-UP lentiviruses (referred to as Hpgd-UP and STAT3-UP, respectively) were constructed using HEK293T cells (CBP60661, Nanjing Kebai Biotechnology Co., Ltd., Nanjing, China). A control lentivirus (referred to as NC-UP) was also constructed.

Plasmid and lentivirus packaging services were provided by Bioengine. HEK293T cells were co-transfected with pre-constructed plasmids carrying a single luciferase reporter gene (NC-UP-luc, Hpgd-UP-luc, and STAT3-UP-luc) and auxiliary plasmids using Lipofectamine 2000 reagent (11668030, Thermo Fisher, Waltham, MA, USA). Lentivirus was obtained after validation, amplification, and purification.

To perform lentivirus-mediated cell transfection, 5×10^5 cells were seeded into a 6-well plate. Once the cell confluence reached 70%–90%, an appropriate quantity of lentivirus packaging (multiplicity of infection (MOI) = 10, with a working titer of approximately 5×10^6 TU/mL) and 5 μg/mL of polybrene (TR-1003, Merck, Rahway, NJ, USA) were introduced to the transfection medium. After transfection for 4 h, an equal medium volume was added to dilute polybrene. After a further 24 h, fresh medium was substituted. Transfection status was assessed after 48 h using a luciferase reporter gene, and a suitable concentration of puromycin (A1113803, Gibco, Grand Island, NY, USA) was utilized for resistant selection to acquire stably transfected cell lines. The cells were collected at the point where cell death ceases in the medium comprising purine mycophenolate and subsequently the efficiency of overexpression was ascertained through RT-qPCR and Western blot analysis.

2.20. Cell Counting Kit-8 (CCK-8)

The 96-well plate was seeded with a cell density of 5×10^3 BV2 cells, and the cells were subsequently incubated in a humidified incubator at 37 °C. After 1 h, the absorbance of each well at 450 nm was recorded using the Micro-plate Reader (abx700005, Beijing Qiwei Yicheng Technology Co., Ltd., Beijing, China) [19].

2.21. 3-(4,5-Dimethylthiazol-2-yl)-2,5-diphenyltetrazolium bromide (MTT) assay to evaluate cell viability

Cells were inoculated in a 96-well plate at a density of 1×10^4 cells per well using a culture medium, followed by incubation for 24 h. After the cells from different treatment groups with 0.5 mg/mL MTT (298-93-1, Sigma Aldrich, St. Louis, MO, USA) were incubated in the culture medium for 4 h, the MTT solution was removed from each well. Then, 100 μL of dimethyl sulfoxide (DMSO; 67-68-5, Sigma Aldrich, St. Louis, MO, USA) or any other appropriate solvent was added to fully dissolve the resulting purple formazan crystals. Cell viability was assessed by measuring the absorbance at 570 nm using an enzyme-linked immunosorbent assay (ELISA) reader.

2.22. Scratch migration test

BV2 cells were cultured in a 24-well plate. A sterile 200 μL pipette tip was used to create a scratch in the center of each well. Subsequently, the wells were washed with PBS to eliminate any cellular debris that may have been damaged. Cells migrating into the scratching area were imaged at different time intervals (6, 12, and 24 h). Subsequently, the ImageJ software was used to measure the percentage of area occupied by these cells [20].

2.23. Determination of phagocytic activity

BV2 cells were seeded at a density of 1×10^4 cells per well in a 96-well plate to assess the phagocytic activity of microglial cells. Subsequently, they were incubated with pHrodo™ Green *Escherichia coli* (*E. coli*) (P35366, Invitrogen™, Thermo Fisher, Waltham, MA, USA) at a 0.125 mg/mL concentration for 6 h. Furthermore, phagocytized particles could be quantified by measuring fluorescence excitation and emission at 509/533 nm. Moreover, the cells containing fluorescent bio-particles were visualized using a fluorescent microscope and quantified with ImageJ software.

2.24. Mitochondrial reactive oxygen species (ROS) detection

Intracellular ROS was quantified using dihydroethidium (DHE; 104821-25-2, Bio-fount, Beijing, China). BV2 cells were treated with LPS (100 ng/mL, 24 h). Next, the cells were incubated with 2 μM DHE at 37 °C for 30 min. Following incubation, the cells were washed twice with PBS and the cell nuclei were stained with DAPI for 10 min. The fluorescence intensity was observed, and images were captured using a fluorescence microscope [21].

2.25. 5,5',6,6'-Tetrachloro-1,1',3,3'-tetraethylbenzimidazolylcarbocyanine iodide (JC-1) staining

BV2 cells were inoculated at a density of 2×10^4 cells per 35 mm culture dish and cultured overnight. The cells were subjected to various treatments the following day and then divided into groups for 24 h of processing. The cells were washed three times with 1× PBS and then incubated at 37 °C for 20 min with JC-1 dye (T3168, Thermo Fisher, Waltham, MA, USA). After being washed with 1× PBS, the cells were transferred onto a slide for observation using a fluorescence microscope [22].

2.26. Automatic image capture

Proteins tagged with fluorescence were transiently transfected into individual neurons in culture to enable long-term monitoring. The Zeiss Observer Z1 microscope (Carl Zeiss AG, Oberkochen, Germany) was used to track neuronal cultures longitudinally, with imaging conducted every 24 h to assess neuronal survival rates. The microscope software facilitated automated image capture using a 10× long-distance objective lens. It performed various tasks such as identifying specific neuronal regions, auto-focusing, capturing images, and moving to the next non-overlapping region seamlessly. This allowed for efficient scanning of multiple neuron regions on each slide. Once the entire image set was captured, the petri dish was returned to the incubator for subsequent scans. In typical survival experiments, each well had 10 positions, with 4 wells assigned to each condition in a randomized manner to ensure unbiased neuron selection. To monitor the same neural regions across experiments, a template with consistent initial spatial positions was employed.

2.27. Flow cytometry

The cell death rate was detected through flow cytometry using a Beckman Coulter instrument (Beckman Coulter Life Sciences, Brea, CA, USA). In summary, neurons were collected at a density of 1×10^5 cells per well. They were washed with cold PBS and stained with the detection reagent kit (APOAF-20TST, Sigma-Aldrich, St. Louis, MO, USA) without light for 15 min. Subsequently, the sediment was resuspended in 400 μL of binding buffer and stained with 5 μL of Annexin-V using the provided detection reagent from the assay kit. Subsequently, the cells were analyzed using the Novocyte Flow Cytometer (ACEA Biosciences Inc., San Diego, CA, USA).

2.28. Electrophysiological recording

The Axopatch 700B amplifier (pCLAMP10 data acquisition software from Molecular Devices (San Jose, CA, USA)) was used in conjunction with the Digidata 1322A digitizer (also from Molecular Devices (San Jose, CA, USA)) for whole-cell voltage and current clamp recordings. To measure action potentials (AP), a glass electrode was inserted into the intracellular solution. The solution contained the following components: 120 mM K-gluconate (299-27-4, Sigma Aldrich, St. Louis, MO, USA), 15 mM KCl (7447-40-7, Sigma Aldrich, St. Louis, MO, USA), 10 mM HEPES (7365-45-9, Sigma Aldrich, St. Louis, MO, USA), 4 mM Mg-ATP (74804-12-9, Sigma Aldrich, St. Louis, MO, USA), 0.3 mM Tris-GTP (103192-46-7, Sigma Aldrich, USA), and 0.5 mM EGTA (67-42-5, MCE, Monmouth Junction, NJ, USA). The pH of the solution was 7.3. Action potentials were induced by injecting current pulses in current clamp mode. The current varied from -150 to $+290$ pA with increments of 10 pA. This study aims to compare the spike counts generated by current injections in various groups of neurons, with action potential analysis performed using Igor Pro.

2.29. Statistical analysis

The study utilized R language version 4.2.1 and was compiled using the integrated development environment RStudio, version 2022.12.0-353. All data were analyzed using GraphPad Prism 8.0. Continuous variables were presented as mean ± standard deviation (SD). A non-paired *t*-test was employed to compare two groups, while a one-way analysis of variance (ANOVA) was used for comparing multiple groups. A *P*-value of less than 0.05 indicates a statistical difference between the two groups.

3. Results and discussion

3.1. Distinct gut microbiota diversity and composition in NAFLD patients compared to healthy controls

Hepatic encephalopathy is the most prevalent liver complication in patients with advanced stages (F3/F4) of NAFLD [23]. To enhance comprehension of the underlying mechanisms, this study initially acquired 16S rRNA sequencing data for NAFLD from the EMBL-EBI database (https://www.ebi.ac.uk/) using the bio-project accession number PRJNA860335. Six NAFLD patients and six healthy individuals were randomly selected as controls. Alpha-diversity and beta-diversity were assessed through sequence alignment. Alpha-diversity is a method used to measure the species composition within a sample, encompassing information about the number of species present and their relative abundance.

Significant differences were found in the alpha-diversity indices, namely the richness index and Chao1 index, between the NAFLD and control groups in the fecal samples (Figs. 1A and B). The results of the rarefaction curve indicate that the abundance of gut microbiota in the NAFLD group is higher than that in the control group (Fig. 1C).

The α-diversity of bacterial communities in terms of intestinal microbiome abundance and diversity was measured using the Shannon index and ACE index (Figs. S1A and B). The results above indicate notable differences in gut microbiota alpha diversity between the two groups.

Beta diversity is a method used to investigate the variations in species composition among different communities. Three common similarity/distance indices, namely Bray-Curtis, Jaccard, and Manhattan, were employed to calculate the Beta diversity distance matrix. Principal coordinates analysis (PCoA) based on the Bray-Curtis distance showed a distinct separation between the two sample groups (Fig. 1D).

Subsequent analysis of species composition was performed, and the R software package edgeR was used to calculate the discrepancies in gut microbiota abundance among the three groups. The Manhattan plot displayed noteworthy distinctions in operational taxonomic units (OTUs) at the Phylum level between the NAFLD and control groups (Fig. S1C). When simultaneous heatmaps were drawn, the NAFLD group exhibited a depletion of 30 OTUs and an enrichment of 2 OTUs, compared with the healthy control group (Fig. 1E).

Furthermore, we analyzed species composition, encompassing the levels of Kingdom, Phylum, Class, Order, Family, and Genus. In addition to the boundary, there are notable variances in species composition across the remaining five levels. Differences in the species composition of the gut microbiota between NAFLD patients and healthy controls were observed at the phylum level. The NAFLD group had a higher abundance of *Bacteroidetes*, while the healthy group had a higher abundance of *Firmicutes* (Fig. 1F).

At the class level, *Bacteroidia* are more abundant in the NAFLD group, whereas *Clostridia* are more abundant in the healthy group (Fig. 1G). At the order level, *Bacteroidales* are more prevalent in the NAFLD group, whereas *Clostridiales* are more prevalent in the healthy group (Fig. 1H). At the family level, the abundance of *Bacteroidaceae* is higher in the NAFLD group, whereas the healthy group shows a higher abundance of *Ruminococcaceae* (Fig. 1I). At the genus level, it was found that *Prevotella* was more abundant in the NAFLD group, whereas *Agathobacter* was more abundant in the healthy group (Fig. 1J). The differences in species abundance across five levels were calculated and displayed using the STAMP software. Figs. 1K and S1D−F depicts the results.

To conclude, there are notable disparities in gut microbiota diversity between the healthy and NAFLD groups. In the NAFLD group, the abundance of *Bacteroides* is higher, whereas the abundance of *Firmicutes* is lower.

3.2. Alterations in gut microbiota composition and functional pathways in NAFLD patients compared to healthy individuals

Significant differences exist in gut microbiota composition between the normal control group and individuals with NAFLD. Analysis revealed an increase in *Bacteroides* in the NAFLD group. To further investigate the differences in species composition between the two groups of intestinal microbiota, we focused specifically on the genus level and performed LEfSe analysis. The LEfSe analysis results demonstrated that using an LDA score (log10) threshold of >2, the relative abundance of *Bacteroidales*, *Bacteroidia*, and *Bacteroidetes* in the fecal samples of patients in the NAFLD group was higher than in the healthy group. Conversely, the relative abundance of *Peptostreptococcaceae* and *Firmicutes* in the fecal samples of patients in the healthy group was higher compared to the NAFLD group (Figs. 2A and B).

Our study employed PICRUSt for functional prediction and conducted KEGG enrichment analysis. The results showed associations between metabolism, environmental information processing, and organic systems (Fig. 2C). Furthermore, we compared the NAFLD group with the healthy group regarding three pathways. Our findings revealed that metabolism and organic system pathways were upregulated in the NAFLD group, whereas the environmental information processing pathway was downregulated (Fig. 2D).

The results above demonstrate disparities in the levels and compositions of gut microbiota between individuals with NAFLD and those who are healthy. In particular, NAFLD is characterized by an elevated abundance of *Bacteroides* and a reduced level of *Firmicutes*.

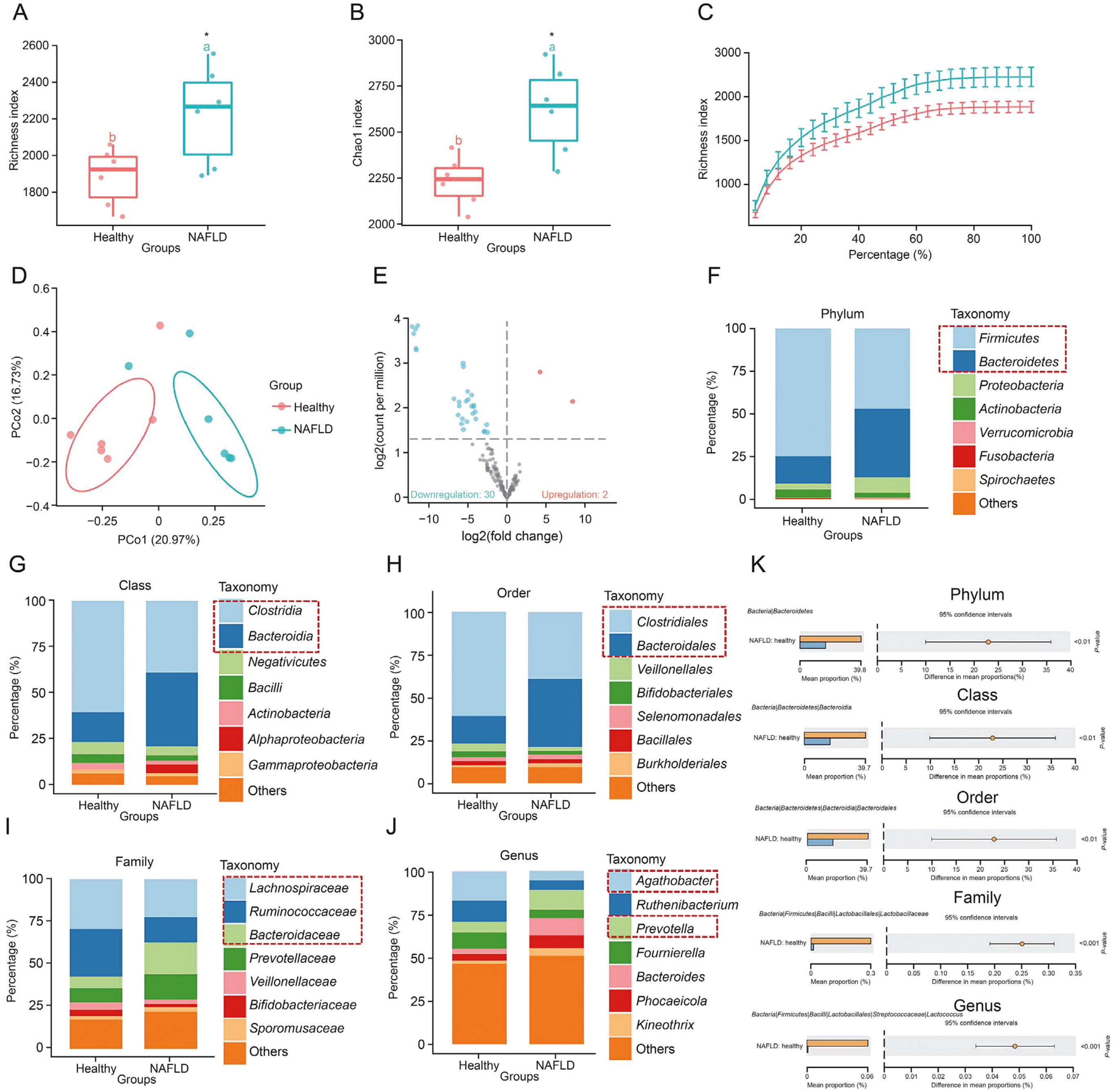

Fig. 1. Analysis of the intestinal microbiota alpha diversity and beta diversity in patients with non-alcoholic fatty liver disease (NAFLD) and healthy controls. (A, B) Alpha diversity analysis of the intestinal microbiota in NAFLD and normal control groups: the richness index (A) and the Chao1 index (B). The letters a and b stand for Shannon and abundance-based coverage estimator (ACE) indices, respectively. (C) Alpha rarefaction curves of the intestinal microbiota in normal controls and NAFLD patients. (D) Beta diversity analysis of the intestinal microbiota in normal controls and NAFLD patients. (E) Volcano plot comparing the abundance differences between normal controls and NAFLD groups. (F–J) Stacked bar charts showing the relative abundance of intestinal microbiota at the phylum (F), class (G), order (H), family (I), and genus (J) levels, with different colors representing different phyla. (K) Analysis of species abundance differences at the phylum, class, order, family and genus levels, displaying the most entries. Healthy group ($n = 6$) and NAFLD group ($n = 6$). $^{*}P < 0.05$. PCo: principal coordinates.

3.3. HFD induces NAFLD in mice with accompanying liver pathology and cognitive impairments

By conducting 16S data analysis using public databases, we observed a substantial rise in the abundance of *Bacteroides* in the fecal samples of patients with NAFLD. To gain a deeper understanding of the molecular mechanisms underlying liver-intestine circulation, this study initially implemented an HFD to induce a model of fatty liver in BALB/c mice. Male mice were housed in the same cage and provided either an HFD or an ND. We observed that HFD mice experienced rapid weight gain within the first 8 weeks, followed by a slower growth rate from 8 to 24 weeks (Fig. 3A).

The body weight of the mice was subsequently assessed every 8 weeks. It was observed that the liver weight of the mice increased from the 8th week onwards after being fed an HFD. Additionally, the growth rate accelerated between weeks 16 and 24 (Fig. 3B).

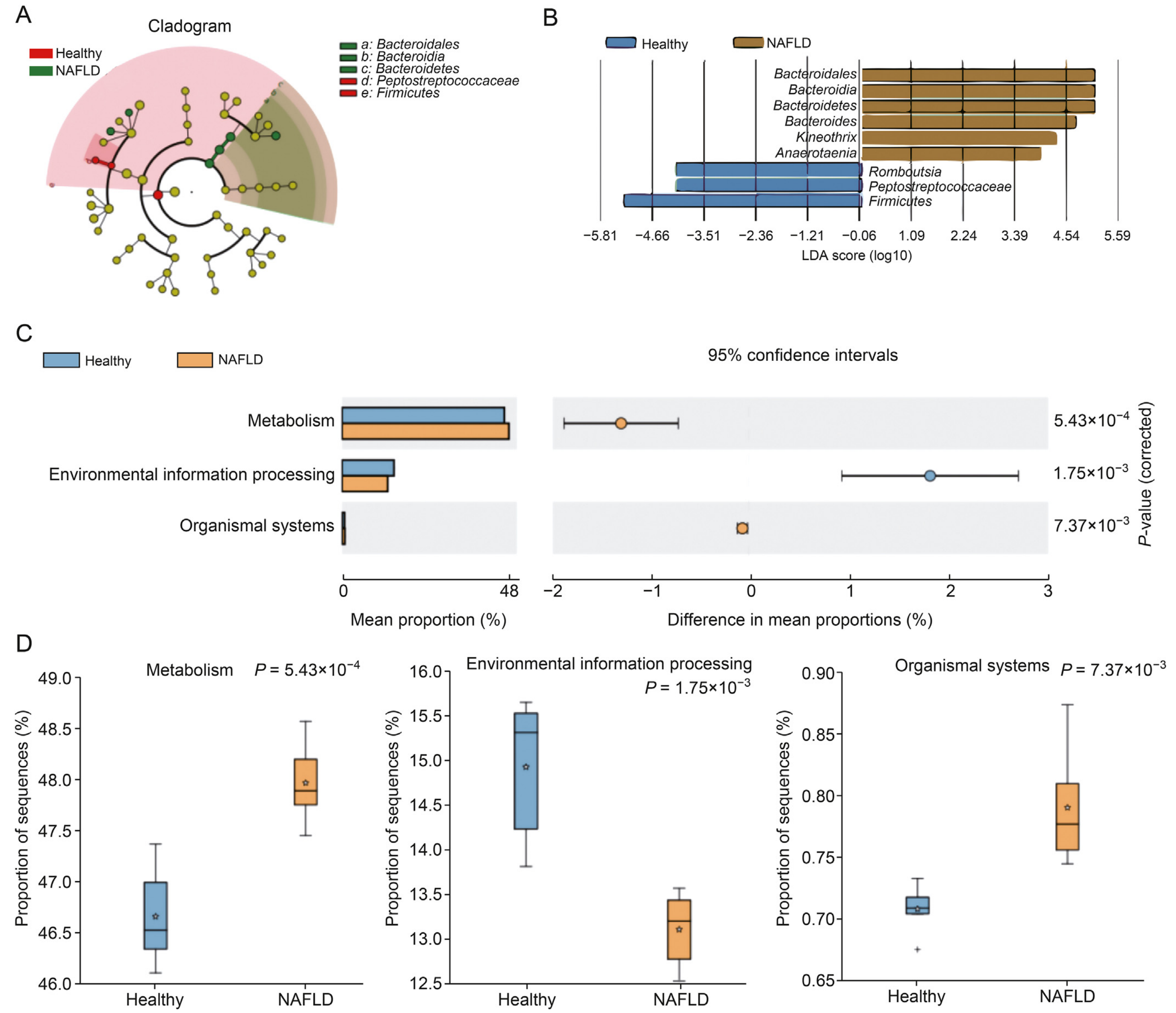

Fig. 2. Analysis of the composition and functional characteristics of the gut microbiota in non-alcoholic fatty liver disease (NAFLD) patients based on linear discriminant analysis effect size (LEfSe) and phylogenetic investigation of communities by reconstruction of unobserved states (PICRUSt). (A) Phylogenetic tree of species abundance of the gut microbiota in NAFLD and normal control groups, where inner to outer circles represent classification levels from species to genus, and the diameter represents the relative abundance, yellow nodes represent species with no differences, red nodes represent microbial groups with higher abundances in the normal group, and green nodes represent microbial groups with higher abundances in the NAFLD group. (B) Bar chart showing the linear discriminant analysis (LDA) value distribution of species abundance in the gut microbiota of NAFLD and normal control rats. Healthy group ($n = 6$) and NAFLD group ($n = 6$). (C) Kyoto Encyclopedia of Genes and Genomes (KEGG) functional enrichment prediction using PICRUSt. (D) Bar chart showing the differences in three pathways.

Upon visual observation of the external shape of the mouse liver, it becomes evident that starting from the 8th week, the liver size gradually increases. The liver of mice on an ND displays a reddish-brown coloration, whereas HFD diet mice exhibit yellow or yellowish-brown changes in their livers starting from the 8th week. Moreover, the liver tissue experiences a decrease in hardness, resulting in a softer texture (Fig. 3C).

Histological staining indicated that the livers of mice fed an HFD for 8 weeks displayed a central-peripheral pattern of fatty degeneration. Moreover, as the feeding duration increased, there was a gradual rise in macrovesicular steatosis, which ultimately extended to the portal vein area of the liver (Fig. 3D).

From the 8th week onwards, the serum levels of ALT, AST, and TAG in mice showed an increase. Moreover, the LDL-C/HDL-C ratio increased starting from the 8th week (Figs. 3E–H). Furthermore, the expression of Cidec, a protein associated with lipid droplets, increased in the liver tissue at multiple time points, particularly at week 8 (Figs. 3I and J).

The data above indicate that an HFD could lead to the development of NAFLD. NAFLD could be observed in mice as an early-stage model after 8 weeks on the HFD, while a late-stage model could be seen after 24 weeks on the HFD.

While administering the HFD to the mice, it became apparent that they displayed different levels of depressive-like behavior over time. Hence, behavioral experiments were conducted on mice to investigate their motor abilities. The decline in motor abilities was observed from the 16th week in the OFT, which was employed to assess their exploratory and locomotor skills. The mice exhibited

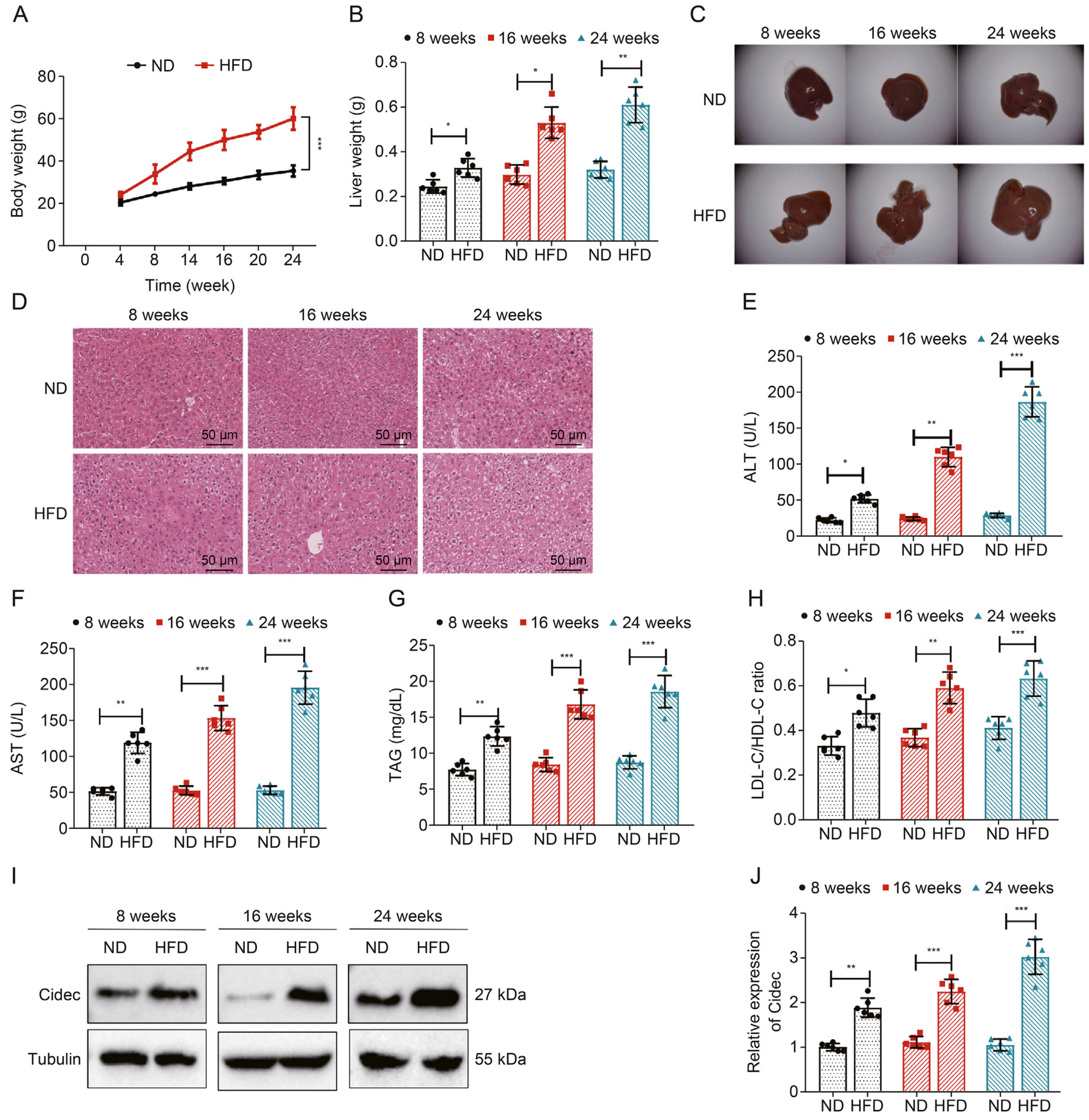

Fig. 3. Induction of non-alcoholic fatty liver disease (NAFLD) mouse model by high-fat diet (HFD) feeding. (A, B) Changes in body weight (A) and liver weight (B) from 4 to 24 weeks in mice fed a normal diet (ND) and an HFD. (C) Representative liver images at 8, 16, and 24 weeks in mice fed a ND and an HFD. (D) Hematoxylin and eosin (H&E) staining of liver tissues. (E–H) Measurement of serum levels of alanine transaminase (ALT) (E), aspartate transaminase (AST) (F), triacylglycerol (TAG) (G), and low-density lipoprotein cholesterol (LDL-C)/high-density lipoprotein cholesterol (HDL-C) ratio (H) in mice. (I–J) Western blot analysis of lipid droplet protein expression in liver tissues (I) and the statistical graph (J). Each group of mice consisted of six individuals, and the values are presented as means ± standard deviation (SD). $^{*}P < 0.05$, $^{**}P < 0.01$, and $^{***}P < 0.001$.

reduced movement capabilities, evidenced by decreased average movement speed, total distance traveled, and number of passages (Figs. 4A–D). The duration of time spent in the central region is longer, whereas the distance covered is shorter (Figs. 4E and F). The mice displayed depressive responses after being fed an HFD for 16 weeks.

Simultaneously, the MWM test assessed the spatial learning and memory capacities of mice fed an HFD for 16 weeks. Notably, the control group demonstrated a shorter escape latency. Distinctions in spatial learning became evident as early as the 4th day of training (Fig. 4G), with the HFD mice displaying a longer escape latency. When the swimming speed is controlled (Fig. 4H), mice on an HFD exhibit shorter visit durations and fewer visits in the target quadrant. These findings suggest impaired spatial memory (Figs. 4I–K).

We discovered that mice with HFD-induced NAFLD also experienced concurrent brain dysfunction.

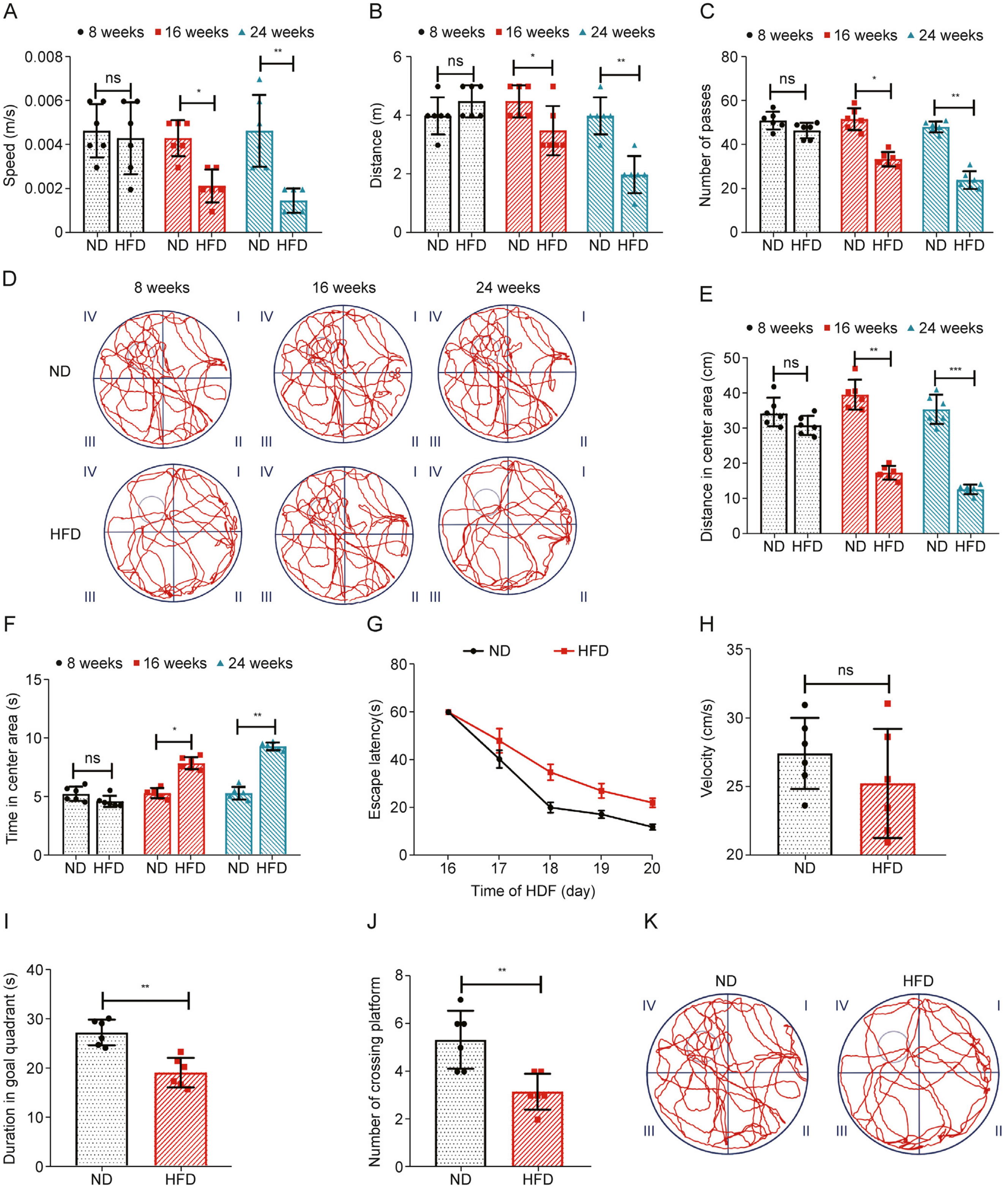

Fig. 4. Behavioral analysis in non-alcoholic fatty liver disease (NAFLD) mice. (A–F) Open field test (OFT), including average speed (A), traveled distance (B), number of crossings (C), representative trace in test (D), distance traveled in the center area (E), and time spent in the center area (F). (G–K) Morris water maze (MWM) test, including escape latency during the 5-day training period (G), average speed in the spatial probe test (H), duration in goal quadrant (I), and visit frequency (J) in the quadrant where the platform was previously located, and representative trace in the spatial probe test (K) (the platform was previously located in the center of quadrant IV). Each group of mice consisted of six individuals, and the values are presented as means ± standard deviation (SD). $^{*}P < 0.05$, $^{**}P < 0.01$, and $^{***}P < 0.001$. ns: no difference.

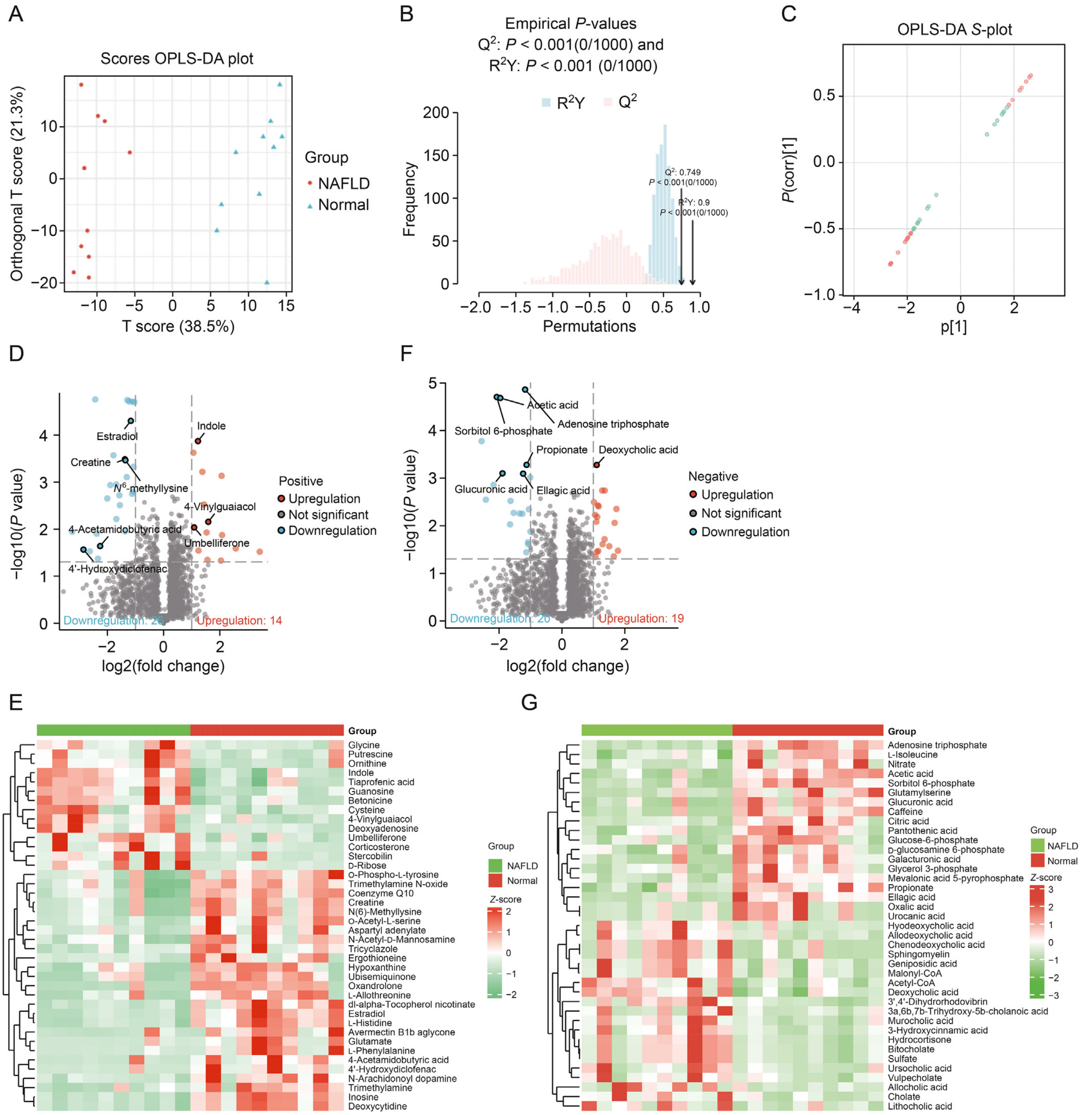

Fig. 5. Metabolomic analysis of differential metabolites between non-alcoholic fatty liver disease (NAFLD) and normal mice. (A) Orthogonal partial least squares discriminant analysis (OPLS-DA) score plot in positive ion mode, where the *x*-axis represents predictive component scores and the *y*-axis represents orthogonal component scores, and the percentage indicates the explanatory power of the components. (B) OPLS-DA validation plot in positive ion mode, where the *x*-axis represents model R^2Y and Q^2 values, and the *y*-axis represents the frequency of model classification efficacy in 200 random permutation experiments. The orange represents random grouping model R^2Y, purple represents random grouping model Q^2, and black arrows represent R^2X, R^2Y, and Q^2 values of the original model. (C) *S*-plot of OPLS-DA in positive ion mode, where the *x*-axis represents the covariance between principal components (PCs) and metabolites, and the *y*-axis represents the correlation coefficient (*r*) between principal components and metabolites. The red dots represent metabolites with variable importance in projection (VIP) values greater than or equal to 1, and green dots represent metabolites with VIP values less than 1. (D, E) Volcano plot (D) and heat map (E) of differential metabolites in positive ion mode (normal group, $n = 10$ and NAFLD group, $n = 10$). (F, G) Volcano plot (F) and heat map (G) of differential metabolites in negative ion mode (normal group, $n = 10$ and NAFLD group, $n = 10$).

3.4. Differential gut metabolomic profiles in NAFLD mice revealed by LC-MS analysis

Behavioral manifestations of cognitive dysfunction in mice were observed during NAFLD induction. We collected 10 NAFLD and 10 samples of normal mouse feces for untargeted metabolomic analysis using LC-MS.

An orthogonal partial least squares-discriminant analysis (OPLS-DA) model was generated to visualize group separation based on differential metabolite profiles. Our experimental results indicate a

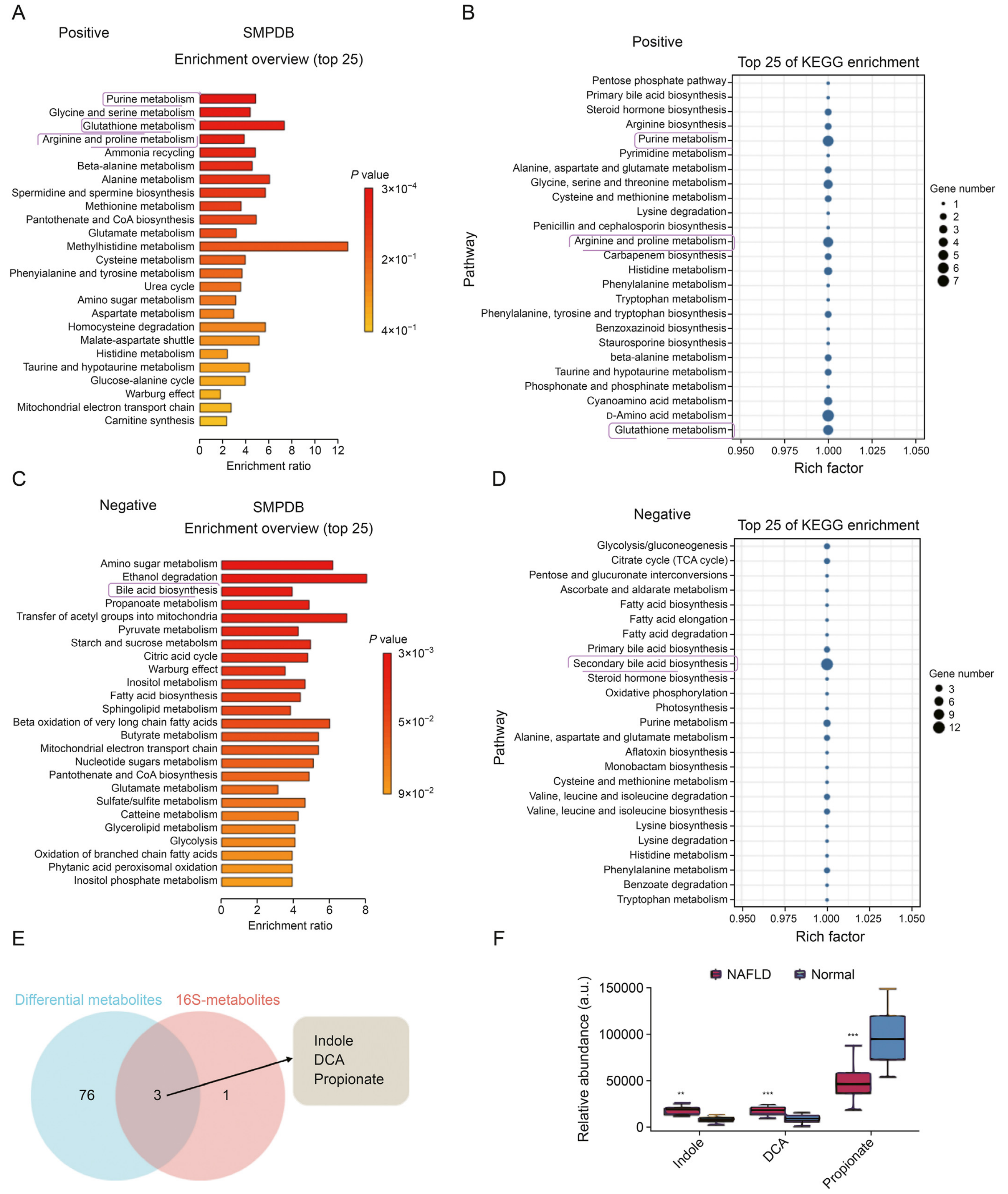

Fig. 6. Metabolic differences and potential mechanisms between non-alcoholic fatty liver disease (NAFLD) mice and normal mice. (A, B) Enrichment analysis of differential metabolites in the MetaboAnalyst database under positive ion mode: Small Molecule Pathway Database (SMPDB) (A) and Kyoto Encyclopedia of Genes and Genomes (KEGG) (B). (C, D) Enrichment analysis of differential metabolites in the MetaboAnalyst database under negative ion mode: SMPDB (C) and KEGG (D). (E) Venn diagram illustrating the intersection between differential metabolites and differential microbiota-related metabolites. (F) Box plots showing differential expression of indole, deoxycholic acid (DCA), and propionate, with the normal group ($n = 10$) and NAFLD group ($n = 10$). Data are presented as mean ± standard deviation (SD). $^{**}P < 0.01$ and $^{***}P < 0.001$. TCA: tricarboxylic acid.

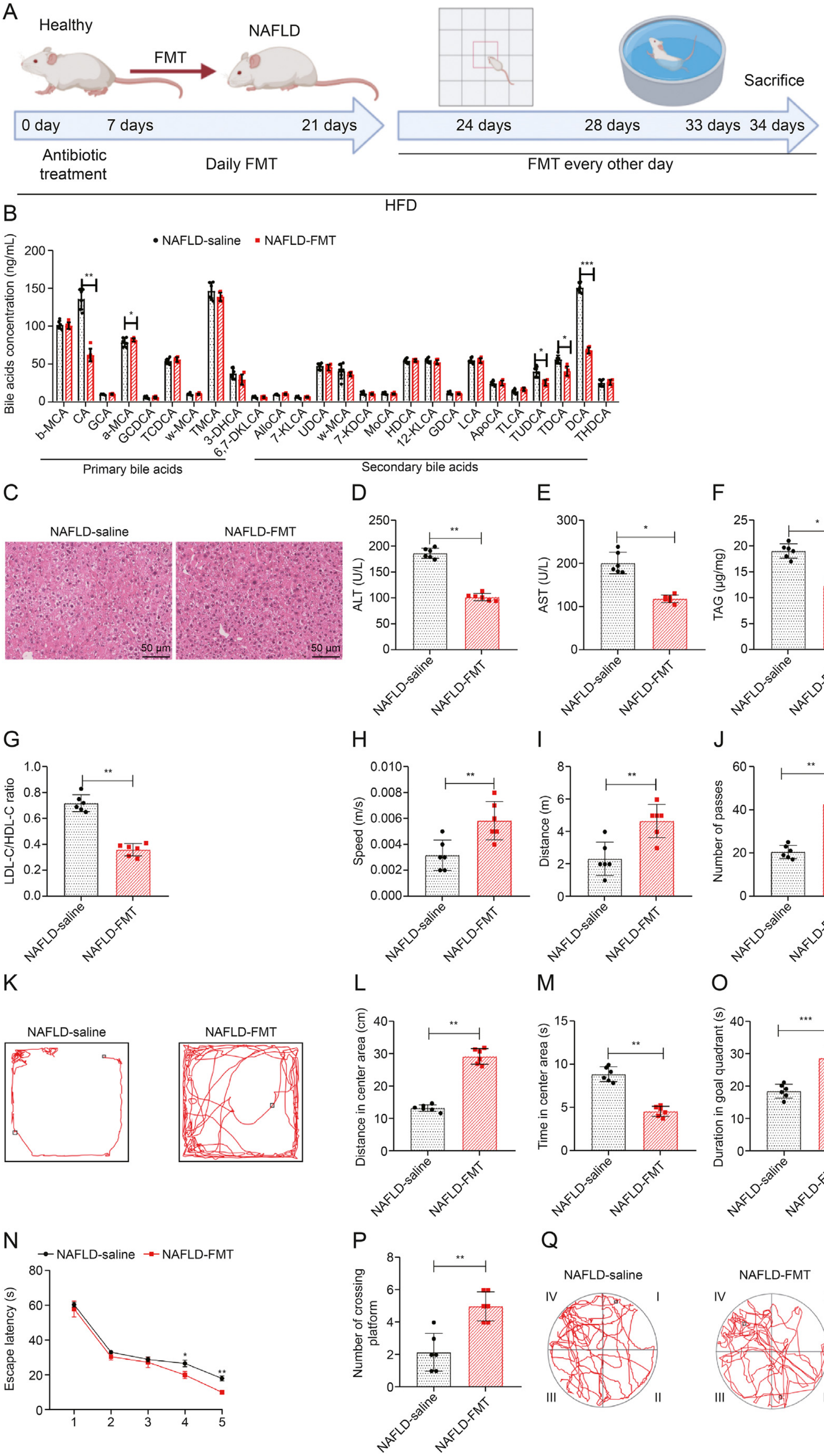
A
Healthy
FMT
NAFLD
Sacrifice
0 day
7 days
21 days
24 days
28 days
33 days
34 days
Antibiotic treatment
Daily FMT
FMT every other day
HFD
B
NAFLD-saline
NAFLD-FMT
Bile acids concentration (ng/mL)
200
150
100
50
0
**
*
***
*
*
b-MCA
CA
GCA
a-MCA
GCDCA
TCDCA
w-MCA
TMCA
3-DHCA
6,7-DKLCA
AlloCA
7-KLCA
UDCA
w-MCA
7-KDCA
MoCA
HDCA
12-KLCA
GDCA
LCA
ApoCA
TLCA
TUDCA
TDCA
DCA
THDCA
Primary bile acids
Secondary bile acids
C
NAFLD-saline
NAFLD-FMT
50 μm
50 μm
D
ALT (U/L)
250
200
150
100
50
0
**
E
AST (U/L)
300
200
100
0
*
F
TAG (μg/mg)
25
20
15
10
5
0
*
G
LDL-C/HDL-C ratio
1.0
0.8
0.6
0.4
0.2
0.0
**
H
Speed (m/s)
0.010
0.008
0.006
0.004
0.002
0.000
**
I
Distance (m)
8
6
4
2
0
**
J
Number of passes
60
40
20
0
**
K
NAFLD-saline
NAFLD-FMT
L
Distance in center area (cm)
40
30
20
10
0
**
M
Time in center area (s)
15
10
5
0
**
O
Duration in goal quadrant (s)
40
30
20
10
0
***
N
NAFLD-saline
NAFLD-FMT
Escape latency (s)
80
60
40
20
0
1
2
3
4
5
*
**
P
Number of crossing platform
8
6
4
2
0
**
Q
NAFLD-saline
NAFLD-FMT
IV
I
III
II
IV
I
III
II
NAFLD-saline
NAFLD-FMT

clear separation in the metabolic profiles between the NAFLD and control groups, suggesting significant alterations in mouse intestinal metabolites due to NAFLD (Fig. 5A).

Further validation of the OPLS-DA evaluation model was performed to assess its effectiveness for inter-group comparison in positive ion mode, yielding R^2Y and Q^2 values of 0.907 and 0.789, respectively. The results of 200 iterations of random permutation testing confirm the efficacy of the OPLS-DA model, as depicted in Fig. 5B.

Using the OPLS-DA results, we identified the distinct metabolites between the two groups based on the variable importance in projection (VIP) from the multivariate analysis OPLS-DA model we generated (Fig. 5C).

Differential metabolites were screened using multivariate analysis and *t*-tests. The volcano plot illustrates the disparities in the filtering outcomes observed between positive and negative ions. Specifically, in the positive ion mode, 41 differential metabolites, consisting of 14 upregulated and 27 downregulated metabolites, were identified (Fig. 5D; Table S3). Hierarchical clustering, combined with Euclidean distance calculations, was employed for the clustering analysis of these differential metabolites. Hierarchical clustering visualizes different metabolites as a heatmap (Fig. 5E). Thirty-nine differential metabolites were generated in the negative ion mode, comprising 19 upregulated and 20 downregulated metabolites (Figs. 5F and G; Table S4). Demonstrate differences in metabolites was observed in the gut between two distinct groups (Tables S5 and S6).

Significant differences in gut metabolism levels between NAFLD and control mice were identified through non-targeted metabolomic evaluation using LC-MS.

3.5. Metabolic pathway analysis reveals key roles of DCA and other differential metabolites in NAFLD development

The study identified substantial metabolic disparities between mice with NAFLD and healthy mice. We conducted a functional enrichment analysis to gain more insights into the potential functions and roles of differentially expressed metabolites. We utilized the MetaboAnalyst 5.0 database for both positive and negative ion modes.

In positive ion mode, the results indicated that the differential metabolites were primarily enriched in pathways, including purine metabolism, glycine and serine metabolism, glutathione metabolism, arginine and proline metabolism, and ammonia recycling, as revealed by the analysis conducted on the Small Molecule Pathway Database (SMPDB) database (Fig. 6A).

The analysis of the KEGG database reveals that the differentially expressed metabolites are predominantly enriched in pathways including purine metabolism, arginine and proline metabolism, cyanoamino acid metabolism, d-amino acid metabolism, and glutathione metabolism (Fig. 6B).

We found that the purine metabolism pathway, glutathione metabolism pathway, and arginine and proline metabolism pathway may be key pathways for the differential metabolites in positive ion mode, based on the enrichment analysis of two databases.

Furthermore, analysis of the SMPDB database in the negative ion mode indicated that the metabolized substances that showed differential expression were primarily found in pathways such as amino sugar metabolism, ethanol degradation, bile acid biosynthesis, propanoate metabolism, and transfer of acetyl groups into mitochondria (Fig. 6C).

The analysis of the KEGG database revealed that the differentially expressed metabolites were predominantly enriched in pathways including glycolysis/gluconeogenesis, citrate cycle (tricarboxylic acid (TCA) cycle), secondary bile acid biosynthesis, and purine metabolism (Fig. 6D). Bile acid biosynthesis plays a crucial role in primary and secondary pathways of bile acid production, impacting the development of NAFLD through the regulation of lipid metabolism, inflammatory responses, and energy balance mechanisms [24]. Therefore, we hypothesize that the bile acid biosynthesis pathway may serve as a vital route for differential metabolite action under negative ion mode.

Significant changes were observed in the abundance of *Bacteroidetes* and *Firmicutes* in NAFLD during the analysis of 16S data. We searched the gutMGene database (Table S7) for metabolites and related genes associated with mouse-derived *Pseudomonas* and *Bacillus* anthracis. The combined metabolites of *Bacteroides* fragilis and *Firmicutes* are known as 16S-metabolins. Three intersecting metabolites are obtained from the intersection of the differential metabolites with positive and negative ions (Fig. 6E). Furthermore, DCA and indole show upregulation, while propionate exhibits downregulation (Fig. 6F). DCA is a secondary bile acid involved in the biosynthesis pathway of bile acids.

Based on the findings mentioned above, it is hypothesized that differential metabolites predominantly regulate the occurrence and development of NAFLD through the metabolic pathway of DCA.

3.6. FMT mitigates NAFLD-induced liver damage and cognitive decline in mice via modulation of bile acids

One of the most recent innovative treatment methods for liver diseases is FMT [25]. Research suggests that bile acids play a role in the gut-liver-brain axis associated with cognition [26]. It also aligns with our findings above.

So, we performed FMT on mice with NAFLD. In summary, the mice received a one-week antibiotic treatment to decrease the bacterial burden in their gut, followed by daily gavage feeding of 1 mL of gut microbiota supernatant for two weeks. During behavior testing, the intestinal microbiota washout fluid was prepared in advance using freshly collected feces from healthy and normal mice. FMT was performed every alternate day. The NALFD group of mice were fed a continuous HFD until euthanasia to preserve the intestinal microbiota composition (Fig. 7A).

GC-MS was used to analyze the levels of circulating bile acids in serum. The serum of FMT mice exhibited reduced levels of secondary bile acids, including DCA and two other secondary bile acids, with DCA showing the most change (Fig. 7B). The average concentration of DCA in the serum samples of six NAFLD mice was

Fig. 7. Therapeutic effect of fecal microbiota transplantation (FMT) on non-alcoholic fatty liver disease (NAFLD)-related brain dysfunction in mice. (A) Schematic representation of the experimental procedure following FMT treatment in mice. (B) Circulating levels of bile acids in the serum. (C) Representative hematoxylin and eosin (H&E) images of liver tissue. (D–G) Measurements of serum alanine transaminase (ALT) (D), aspartate transaminase (AST) (E), triacylglycerol (TAG) (F) levels, and low-density lipoprotein cholesterol (LDL-C)/high-density lipoprotein cholesterol (HDL-C) ratio (G) in mice. (H–M) Open field test (OFT) results, including average speed (H), traveled distance (I), number of passes (J), representative tracks in the test (K), distance traveled in the central area (L), and time spent in the central area (M). (N–Q) Morris water maze (MWM) test results, including escape latency during the escape latency (N), duration in goal quadrant (O), number of crossing platform (P), and representative tracks in the spatial probe test (Q) (the platform was previously located in the center of quadrant IV). Each group consisted of six mice. Data are presented as mean ± standard deviation (SD). $^{*}P < 0.05$, $^{**}P < 0.01$, and $^{***}P < 0.001$. b-MCA: β-muricholic acid; CA: cholic acid; GCA: glycocholic acid; a-MCA: α-muricholic acid; GCDCA : glycochenodeoxycholic acid; TCDCA: taurochenodeoxycholic acid; w-MCA: ω-muricholic acid; TMCA: tauromuricholic acid; 3-DHCA: 3-dehydrocholic acid; 6,7-DKLCA: 6,7-diketo-lithocholic acid; AlloCA: allocholic acid; 7-KLCA: 7-ketolithocholic acid; UDCA: ursodeoxycholic acid; 7-KDCA: 7-ketodeoxycholic acid; MoCA: monohydroxycholic acid; HDCA: hyodeoxycholic acid; 12-KLCA: 12-ketolithocholic acid; GDCA: glycodeoxycholic acid; LCA: lithocholic acid; ApoCA: apocholic acid; TLCA: taurolithocholic acid; TUDCA: tauroursodeoxycholic acid; TDCA: taurodeoxycholic acid; DCA: deoxycholic acid; THDCA: taurohyodeoxycholic acid.

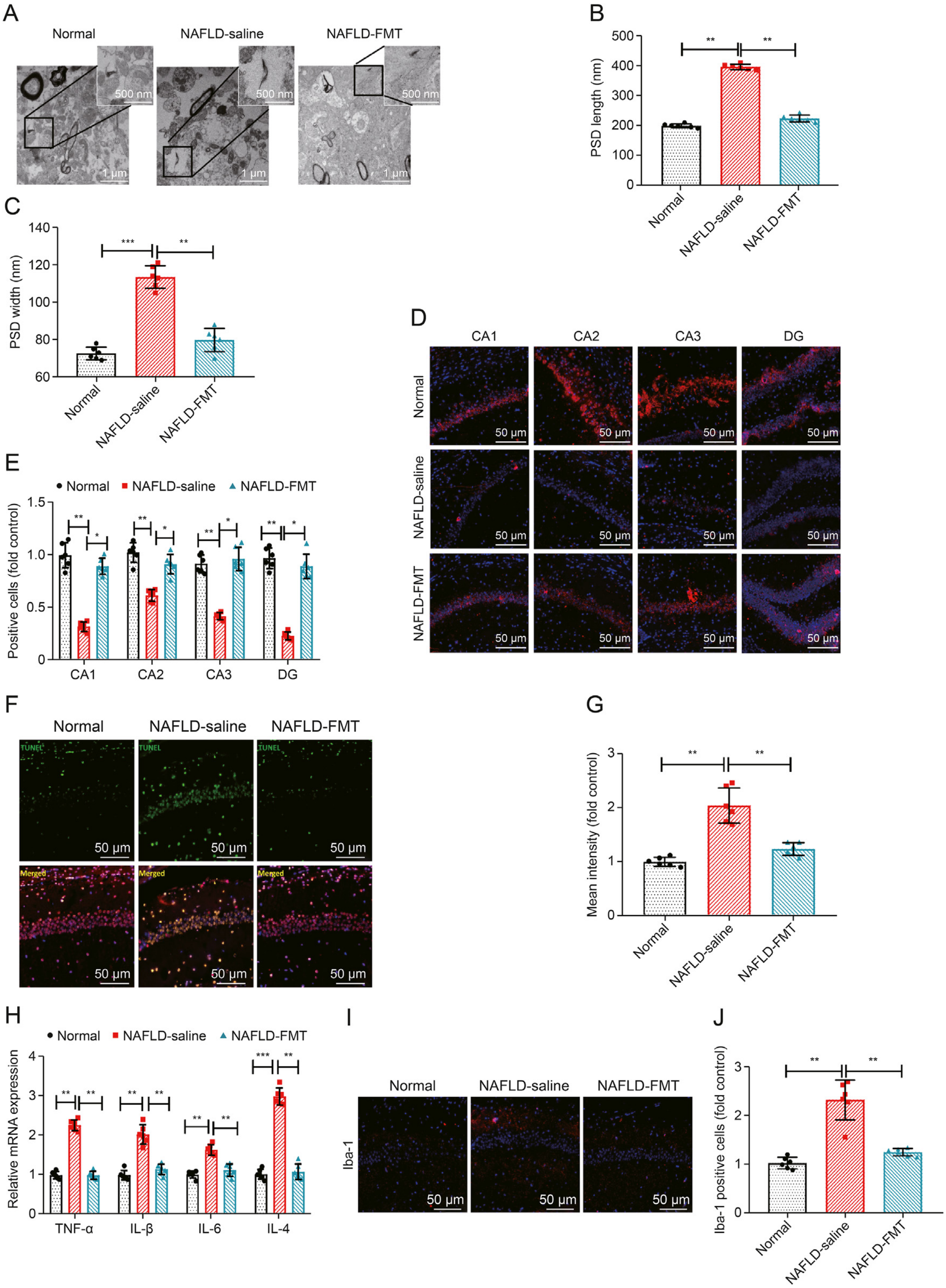

Fig. 8. Effects of fecal microbiota transplantation (FMT) on hippocampal inflammation and neuronal proliferation in non-alcoholic fatty liver disease (NAFLD) mice model. (A) Representative images of synaptic ultrastructure in mouse hippocampal tissue. The insets indicate enlarged regions show the ultrastructural morphology of the postsynaptic density (PSD), with evident thickening and elongation in the NAFLD-saline group, which is alleviated by FMT treatment. (B, C) Length (B) and width (C) of the PSD. (D, E) Quantitative analysis of immunofluorescence staining of hippocampal neurons in different regions (cornu ammonis 1 (CA1), CA2, CA3, and dentate gyrus (DG)) (D) and the statistical graph of average fluorescence intensity (E). (F, G) Terminal deoxynucleotidyl transferase dUTP nick-end labeling (TUNEL) staining of hippocampal neurons (F) and the statistical graph of TUNEL mean intensity (G). (H) Messenger RNA (mRNA) levels of inflammatory cytokines (tumor necrosis factor alpha (TNF-α), interleukin (IL)-1β, IL-6, and IL-4) in the hippocampus. (I, J) Expression levels of microglial cell marker ionized calcium-binding adapter molecule 1 (Iba-1) detected by immunofluorescence staining in the hippocampus (I) and the statistical graph (J). Each group consisted of six mice. Data are presented as mean ± standard deviation (SD). $^{*}P < 0.05$, $^{**}P < 0.01$, and $^{***}P < 0.001$.

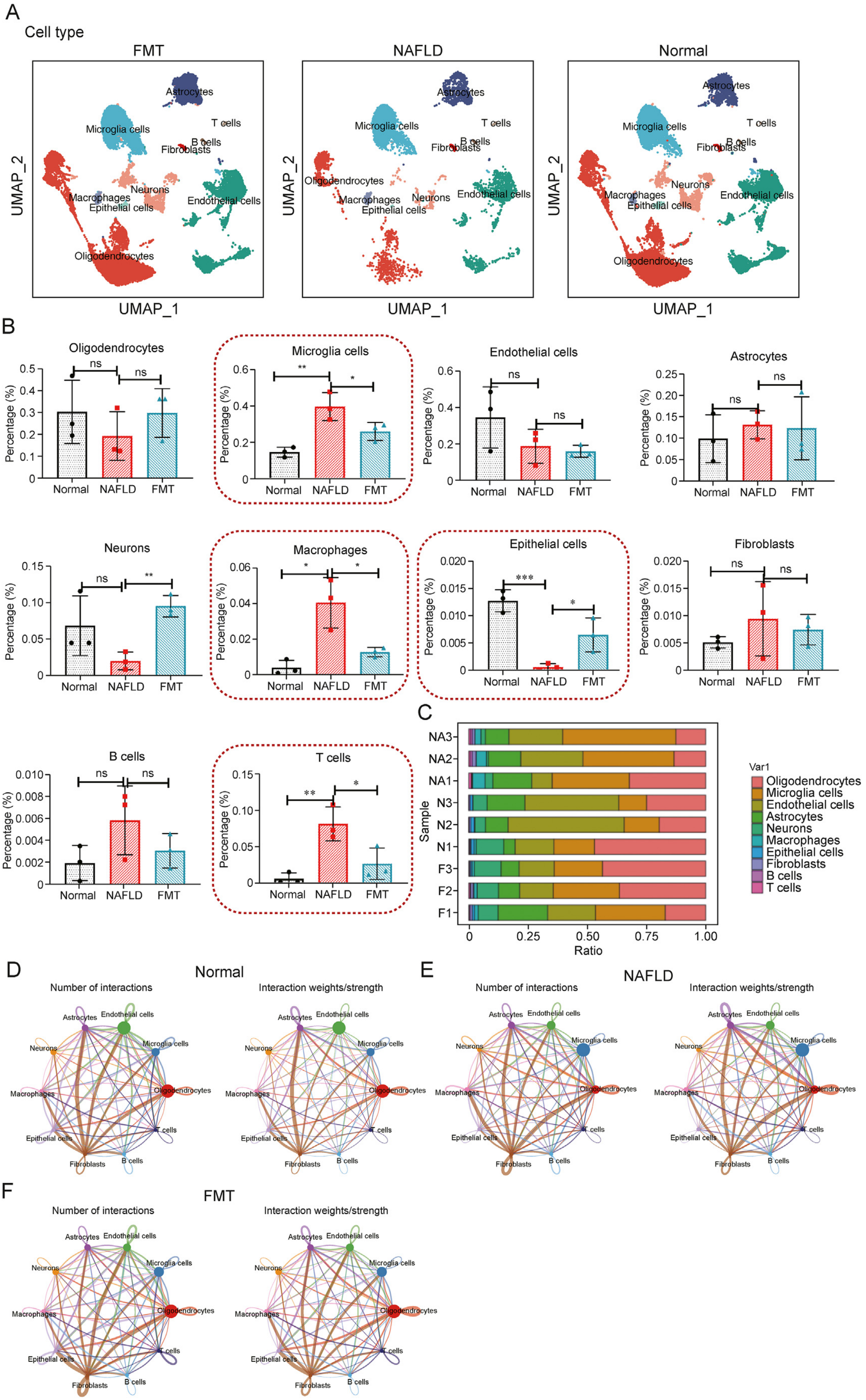
A
Cell type
FMT
NAFLD
Normal
Astrocytes
Microglia cells
T cells
B cells
Fibroblasts
Neurons
Macrophages
Epithelial cells
Endothelial cells
Oligodendrocytes
UMAP_1
UMAP_2
B
Oligodendrocytes
Microglia cells
Endothelial cells
Astrocytes
Neurons
Macrophages
Epithelial cells
Fibroblasts
B cells
T cells
Percentage (%)
Normal
NAFLD
FMT
ns
*
**
***
C
Sample
NA3
NA2
NA1
N3
N2
N1
F3
F2
F1
0
0.25
0.50
0.75
1.00
Ratio
Var1
Oligodendrocytes
Microglia cells
Endothelial cells
Astrocytes
Neurons
Macrophages
Epithelial cells
Fibroblasts
B cells
T cells
D
Normal
E
NAFLD
F
FMT
Number of interactions
Interaction weights/strength

152 ng/mL. Following FMT treatment, the average DCA content decreased to 76 ng/mL.

Histological staining revealed that NALFD-saline mice exhibited liver fibrosis and macrovesicular steatosis in liver tissues compared to NALFD mice treated with FMT (Fig. 7C). The measurement of ALT, AST, TAG, and LDL-C/HDL-C ratio in serum showed that NALFD-FMT mice had better liver function than NALFD-saline mice (Figs. 7D–G), suggesting that FMT could ameliorate fatty liver symptoms in mice.

During behavioral analysis, FMT enhanced the activity levels of NAFLD mice. The increased average speed, total distance, and number of passes (Figs. 7H–K). In contrast, the mice that received FMT exhibited a reduction in the amount of time spent in the central zone and instead traveled longer distances (Figs. 7L and M).

During the MWM experiment, it was observed that the escape latency of NALFD-FMT mice was reduced (Fig. 7N). Additionally, NALFD mice receiving healthy FMT spent more time in the target quadrant and had a higher visit frequency (Figs. 7O–Q), indicating that FMT improved spatial memory deficits.

In summary, our preliminary research findings confirm that FMT could reduce serum levels of DCA in mice with NAFLD, leading to a notable improvement in their liver condition and a reduction in cognitive impairments.

3.7. FMT attenuates NAFLD-induced hippocampal inflammation, microglial activation, and neuronal apoptosis

By treating NAFLD mice models with FMT, we have observed that FMT can potentially decrease DCA levels in mice, effectively improving fatty liver manifestations and spatial memory abilities. Alterations in the hippocampus contribute to age-related cognitive decline and central nervous system diseases [27].

Thus, our focus was on investigating synaptic ultrastructure about cognition and memory. Upon analysis of the postsynaptic density (PSD), it was observed that both the length and width of the PSD increased in the NAFLD group. Conversely, these parameters were reduced by FMT (Figs. 8A–C).

We conducted immunofluorescent staining to analyze the neurons in the hippocampus of each mouse group, which were labeled with NeuN. The mice treated with FMT exhibited increased fluorescence intensity compared to the NAFLD mice (Figs. 8D and E). TUNEL staining further demonstrated that NAFLD led to increased TUNEL-positive cells in the hippocampus. However, treatment with FMT reduced these cell numbers (Figs. 8F and G).

The study detected inflammation markers in the hippocampus, including tumor necrosis factor alpha (TNF-α), interleukin (IL)-1β, IL-6, and IL-4, using RT-qPCR. The results revealed elevated markers in the NAFLD group; however, a statistical decrease was observed following FMT treatment (Fig. 8H). In this study, we conducted further investigation on microglia, which is the primary cell associated with inflammation in the hippocampus. To assess their activity, we measured the expression level of Iba-1, an immunofluorescence marker for microglia. The results demonstrated a substantial increase in positive cells in the NAFLD group; however, there was a decrease following FMT treatment (Figs. 8I and J). This result implies that NAFLD could trigger an inflammatory response in the hippocampus and augment microglial cells.

The data above indicates that FMT can potentially suppress the hippocampus's inflammatory response, decrease microglial cell activation, and inhibit neuronal apoptosis.

3.8. Single-cell transcriptomics reveals FMT-induced cellular and intercellular alterations in the NAFLD mouse hippocampus

The experiments above have demonstrated that FMT could alleviate the symptoms of hepatic encephalopathy in patients with NAFLD. In the meantime, metabolomics revealed elevations of DCA levels in NAFLD mice. Moreover, secondary bile acids were detected in both mice's and humans' brains, indicating their potential ability to traverse the blood-brain barrier [28].

To examine the molecular mechanisms in the hippocampus of mice, we gathered hippocampal tissues from normal mice (labeled as normal), mice with NAFLD that received saline injections (labeled as NAFLD), and mice with NAFLD that underwent FMT. Subsequently, we conducted single-cell RNA sequencing (scRNA-seq) analysis.

The Seurat package was utilized to integrate the data. We initially examined the number of genes (nFeature_RNA), mRNA molecules (nCount_RNA), and the percentage of mitochondrial genes (percent.mt) in all cells of the scRNA-seq dataset. The results indicate that most cells exhibited nFeature_RNA < 5,000, nCount_RNA < 20,000, and percent.mt < 20% (Fig. S2A). After applying these criteria, we removed low-quality cells and obtained an expression matrix that consisted of 18,947 genes and 48,874 cells. The correlation analysis of sequencing depth revealed that in the filtered data, the correlation coefficient (r) between nCount_RNA and percent.mt was -0.27, while the r between nCount_RNA and nFeature_RNA was 0.90 (Fig. S2B). This result suggests that the filtered cell data is of good quality and could be further analyzed.

Subsequently, we conducted further analysis on the filtered cells and identified the top 2000 genes with variance in gene expression for subsequent downstream analysis (Fig. S2C). The sample's cell cycle was calculated using the CellCycleScoring function (Fig. S2D), and the obtained data was subsequently normalized.

Next, we employed principal component analysis (PCA) to reduce the linear dimensionality of the dataset. In this study, we display the heatmaps illustrating the gene expressions of PC_1 to PC_6 (Fig. S2E). Additionally, we are demonstrating the cellular distribution across PC_1 and PC_2 (Fig. S2F). A certain batch effect was detected among the samples.

To mitigate batch effects and enhance the accuracy of cell clustering, we utilized the harmony package for batch correction on the sample data (Fig. S3A). We employed ElbowPlot to arrange the standard deviation of the PCs. The results demonstrated that PC_1 to PC_20 effectively capture the information present in the chosen highly variable genes and possess substantial analytical significance (Fig. S3B). The adjusted results demonstrate that the batch effect of the samples has been successfully mitigated (Fig. S3C).

Next, we employed the uniform manifold approximation and projection (UMAP) algorithm for nonlinear dimension reduction on the initial 20 PCs. All cells were divided into 24 clusters using UMAP cluster analysis (Figs. S3D–E). Subsequently, the Bioconductor/R software package called ‘SingleR’ was employed to automatically

Fig. 9. Analysis of cell quantity differences and cellular pathways. (A) Visualization of cell annotation results based on uniform manifold approximation and projection (UMAP) clustering. (B) P-values of t-test analysis on cell contents among normal, non-alcoholic fatty liver disease (NAFLD), and fecal microbiota transplantation (FMT) samples, with differences highlighted by the red dashed box. (C) Proportions of different cell subsets in each sample, with different colors representing different cell subtypes. (D–F) Cell communication network diagrams in the normal group (D), NAFLD (E), and FMT (F), where the thickness of the lines represents the number of pathways and the strength of the interactions. $^{*}P < 0.05$ and $^{**}P < 0.01$. ns: no difference.

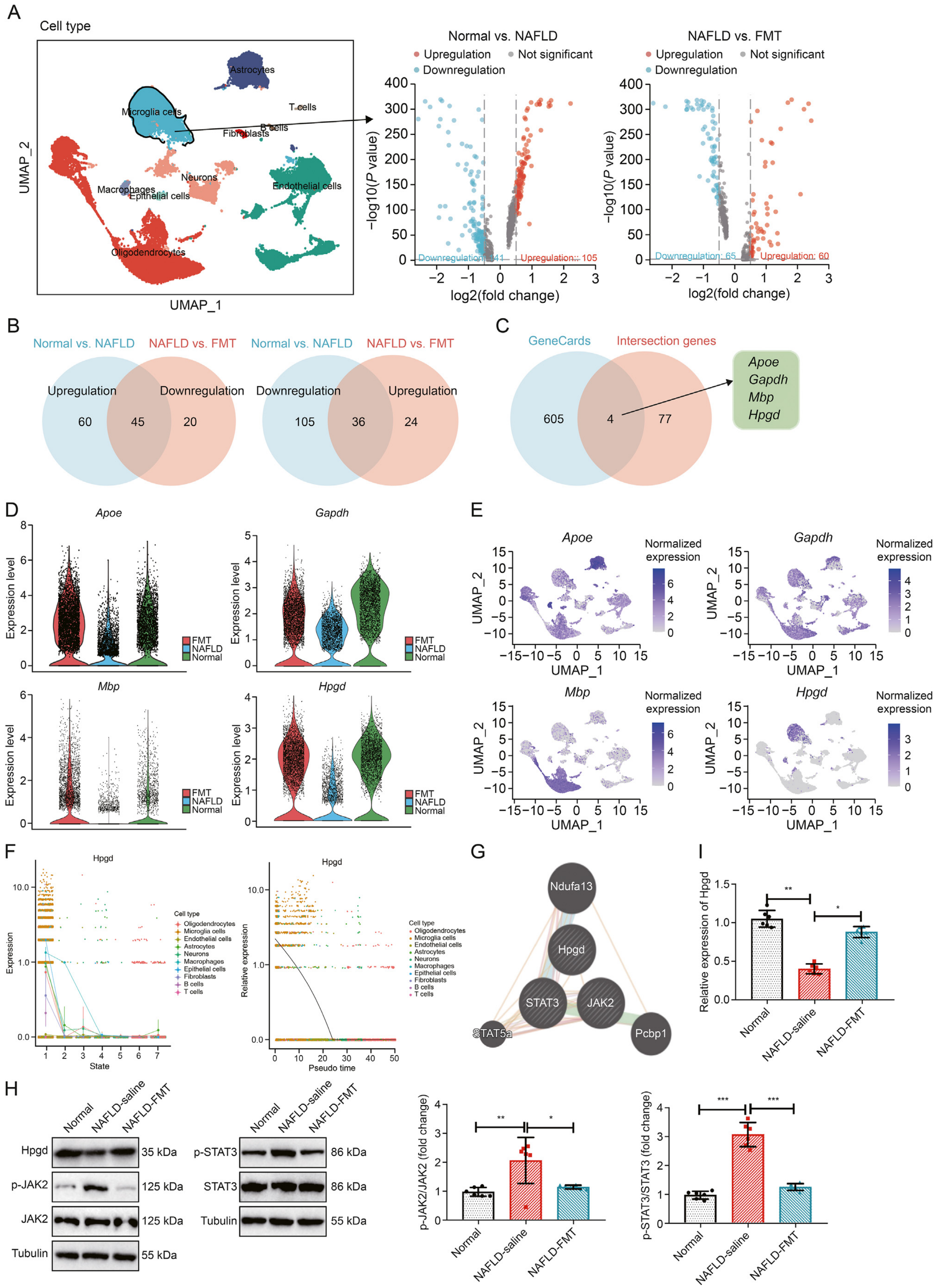
A
Cell type
Astrocytes
Microglia cells
T cells
B cells
Fibroblasts
Neurons
Macrophages
Epithelial cells
Endothelial cells
Oligodendrocytes
UMAP_2
UMAP_1
Normal vs. NAFLD
Upregulation
Not significant
Downregulation
−log10(P value)
log2(fold change)
Downregulation: 141
Upregulation: 105
NAFLD vs. FMT
Downregulation: 65
Upregulation: 60
B
Normal vs. NAFLD
NAFLD vs. FMT
Upregulation
Downregulation
60
45
20
105
36
24
C
GeneCards
Intersection genes
605
4
77
Apoe
Gapdh
Mbp
Hpgd
D
Apoe
Gapdh
Mbp
Hpgd
Expression level
FMT
NAFLD
Normal
E
Normalized expression
UMAP_2
UMAP_1
F
Hpgd
Expression
State
Cell type
Oligodendrocytes
Microglia cells
Endothelial cells
Astrocytes
Neurons
Macrophages
Epithelial cells
Fibroblasts
B cells
T cells
Relative expression
Pseudo time
G
Ndufa13
Hpgd
STAT3
JAK2
STAT5a
Pcbp1
I
Relative expression of Hpgd
Normal
NAFLD-saline
NAFLD-FMT
**
*
H
Hpgd
35 kDa
p-JAK2
125 kDa
JAK2
125 kDa
Tubulin
55 kDa
p-STAT3
86 kDa
STAT3
86 kDa
Tubulin
55 kDa
p-JAK2/JAK2 (fold change)
p-STAT3/STAT3 (fold change)
***

annotate the 24 cell clusters, identifying 10 distinct cell types (Fig. 9A). Furthermore, we have presented the UMAP expression maps for these 10 cell types (Fig. S3F).

Through scRNA-seq analysis, 10 cell types were successfully identified. Using a *t*-test, we conducted a comparative analysis to assess the differences in cell quantity among the normal, NAFLD, and FMT samples. The analysis results indicate that NAFLD samples exhibit a decrease in epithelial cells and a noteworthy increase in microglial cells, macrophages, and T cells compared to normal samples. In contrast to NAFLD, the FMT samples showed an increase in epithelial cells and a decrease in microglia cells, macrophages, and T cells (Figs. 9B and C).

Moreover, to comprehend the functional disparities underlying these quantitative variations, we employed the “CellChat” package in the R language to examine the pathway activity across distinct cells. Variations were observed in the connections among multiple cells (Figs. 9D−F).

Variations in the connection between microglial cells and neurons across different groups could be observed due to changes in the number of microglial cells. These cells are important components in the hippocampus and interact with neurons in intercellular communication.

Using single-cell transcriptomic sequencing, we uncovered the pivotal contribution of FMT in ameliorating brain disorders associated with NAFLD. Additionally, we identified variations in cell subpopulation alterations and intercellular communication within the hippocampus.

3.9. Modulation of microglial activation by FMT: role of hpgd and JAK/STAT signaling in NAFLD-associated brain dysfunction

Significant changes in microglial cells were observed between the normal group and the NAFLD group, as well as between the NAFLD group before and after FMT treatment, based on the analysis above. Subsequently, we analyzed the differential gene expression of microglial cells among distinct groups. There are 246 differentially expressed genes (DEGs) between the normal and NAFLD groups, with 141 showing downregulation and 105 showing upregulation. Additionally, 125 DEGs exist between the NAFLD group and the FMT group, with 65 showing downregulation and 60 showing upregulation (Fig. 10A).

To elucidate the molecular mechanisms underlying the effects of FMT treatment, we conducted an intersection analysis to identify upregulated genes between the normal group and the NAFLD group, as well as between the NAFLD group and the FMT group. This analysis identified 45 genes. Furthermore, we performed an intersection analysis to determine the downregulated genes between the normal and NAFLD groups, as well as between the NAFLD and FMT groups, revealing 36 genes (Fig. 10B).

The genes common to both groups were combined, resulting in a total of 81 genes. Subsequently, we conducted an additional intersection analysis using 609 genes associated with DCA obtained from the GeneCards website. Ultimately, we identified four intersecting genes (Fig. 10C). It is important to note that there is a change in Hpgd, specifically within these two groups in the scRNA-seq dataset (Fig. 10D). Therefore, we have selected Hpgd as the crucial gene for FMT therapy in hepatic steatosis-induced cognitive dysfunction. We generated UMAP plots for these four genes and found that Hpgd appears highly expressed in microglial cells, while the other three genes exhibit a more dispersed distribution (Fig. 10E).

We conducted a pseudotime analysis using the software package “Monocle2”. This analysis allowed us to uncover the migration trajectories of cells in the pseudotime and the various clusters they constitute. We comprehensively investigated the dynamic expression patterns of Hpgd in scRNA-seq datasets. In light of this, we generated a jitter plot illustrating the gene expression levels. We observed a notable increase in Hpgd expression within microglia (Fig. 10F).

Several research reports suggest that HPGD may negatively regulate the STAT3 pathway [29]. The JAK2/STAT3 pathway could activate microglial cells [30]. Thus, we hypothesize that HPGD could hinder the activation of microglial cells by suppressing the JAK/STAT signaling pathway. The relationship between Hpgd, JAK2, and STAT3 in mice was analyzed using the Genemania website. The results demonstrated an interaction between these genes, as illustrated in Fig. 10G.

Western blot technique was employed to assess Hpgd, p-JAK2, JAK2, p-STAT3, and STAT3 expression levels in the hippocampus of mice belonging to distinct groups. The results demonstrated that the expression of Hpgd was lower in the NAFLD group compared to the normal group. The ratio of p-JAK2/JAK2 and p-STAT3/STAT3 was higher. On the other hand, the expression of Hpgd started to increase compared to the NAFLD group. Similarly, the ratio of p-JAK2/JAK2 and p-STAT3/STAT3 was lower (Figs. 10H and I).

Based on the information provided above, it is our tentative speculation that FMT treatment can substantially enhance the expression of Hpgd and mitigate the brain dysfunction resulting from NAFLD by inhibiting the JAK2/STAT3 signaling pathway.

3.10. DCA amplifies microglial activation via hpgd suppression and JAK2/STAT3 signaling augmentation

In the preceding experiment, it was observed that levels of DCA decreased after FMT treatment. Similarly, a decrease in the expression of Hpgd in microglia cells was also noted. Activated microglia, which are essential innate immune cells in the brain, release inflammatory cytokines that cause neurotoxicity in

Fig. 10. Molecular mechanisms of fecal microbiota transplantation (FMT) treatment on non-alcoholic fatty liver disease (NAFLD)-induced brain dysfunction. (A) Volcano plot showing differentially expressed genes (DEGs) in microglial cells between normal and NAFLD samples, and between NAFLD and fecal microbiota transplantation (FMT) samples (normal group, $n = 3$; NAFLD group, $n= 3$; and FMT group, $n = 3$). (B) Venn diagrams showing the overlap of DEGs in microglia between different comparison groups: 45 upregulated genes were commonly identified in both the normal vs. NAFLD and NAFLD vs. FMT comparisons (left) and 36 downregulated genes were commonly shared between the normal vs. NAFLD and NAFLD vs. FMT comparisons (right). These common DEGs may represent key regulators influenced by both disease progression and FMT treatment. (C) Venn diagram of the intersection between deoxycholic acid (DCA)-related genes from GeneCards and genes from Fig. 10B. The diagram shows the overlap between genes associated with DCA identified from the GeneCards database and the intersecting genes from Fig. 10B, with four key genes identified: apolipoprotein E (*Apoe*), glyceraldehyde 3-phosphate dehydrogenase (*Gapdh*), myelin basic protein (*Mbp*), and hydroxyprostaglandin dehydrogenase (*Hpgd*). (D) Violin plots showing the expression levels of the intersecting genes *Apoe*, *Gapdh*, *Mbp*, and *Hpgd*in hippocampal single-cell populations from normal, NAFLD, and FMT groups. (E) Uniform manifold approximation and projection (UMAP) plots depicting the spatial expression distribution of the four intersecting genes (*Apoe*, *Gapdh*, *Mbp*, and *Hpgd*) across all hippocampal cell types. (F) Biased jitter plot showing the expression distribution of Hpgd among different cell types, with the *x*-axis representing cell types and the *y*-axis representing gene expression levels. (G) Prediction of the relationship between Hpgd, Janus kinase 2 (JAK2), and signal transducer and activator of transcription 3 (STAT3) in mouse sources using the Genemania website. (H, I) Protein expression and quantification: representative Western blot images showing expression levels of Hpgd, p-JAK2, JAK2, p-STAT3, and STAT3 in mouse hippocampi (H) and the corresponding semi-quantitative analysis of the p-JAK2/JAK2 and p-STAT3/STAT3 ratios (I), with each group consisting of six mice. Data are presented as mean ± standard deviation (SD). $^{*}P < 0.05$, $^{**}P < 0.01$, and $^{***}P < 0.001$. Ndufa13: nicotinamide adenine dinucleotide (NADH):ubiquinone oxidoreductase subunit A13; Pcbp1: poly(rC)-binding protein 1.

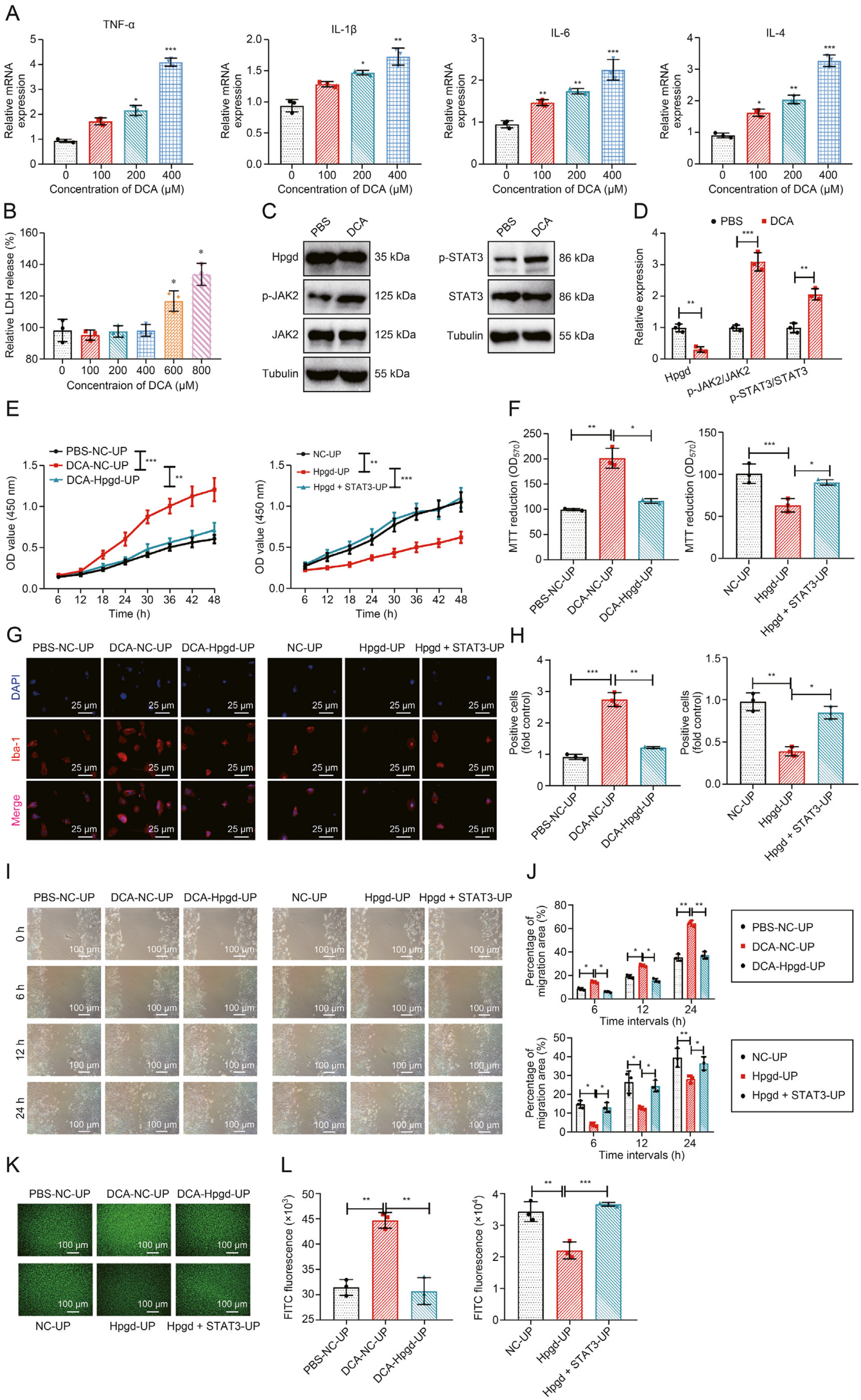
A
TNF-α
IL-1β
IL-6
IL-4
Relative mRNA expression
Concentration of DCA (μM)
0
100
200
400
B
Relative LDH release (%)
Concentraion of DCA (μM)
600
800
C
PBS
DCA
Hpgd
35 kDa
p-JAK2
125 kDa
JAK2
125 kDa
Tubulin
55 kDa
p-STAT3
86 kDa
STAT3
86 kDa
Tubulin
55 kDa
D
PBS
DCA
Relative expression
Hpgd
p-JAK2/JAK2
p-STAT3/STAT3
E
PBS-NC-UP
DCA-NC-UP
DCA-Hpgd-UP
NC-UP
Hpgd-UP
Hpgd + STAT3-UP
OD value (450 nm)
Time (h)
F
MTT reduction (OD570)
G
DAPI
Iba-1
Merge
25 μm
H
Positive cells (fold control)
I
0 h
6 h
12 h
24 h
100 μm
J
Percentage of migration area (%)
Time intervals (h)
K
L
FITC fluorescence (×10³)
FITC fluorescence (×10⁴)
*
**
***

neighboring neurons. This process contributes to the pathogenesis of different brain disorders [31].

Thus, we hypothesize that DCA could activate the JAK2/STAT3 pathway by suppressing Hpgd expression in microglial cells, consequently enhancing microglial cell proliferation and activation.

To verify this hypothesis, we cultured BV2 cells (mouse microglial cells) with various concentrations of DCA, induced the cells with LPS (100 ng/mL), and examined the levels of pro-inflammatory cytokines TNF-α, IL-1β, IL-6, and IL-4 in the cells. The experimental results demonstrate a gradual increase in the expression levels of these factors with the rising concentration of DCA (Fig. 11A).

Additionally, LDH experiments were conducted to examine the cytotoxic impact of DCA. The findings revealed that DCA, at concentrations below 400 μM, did not exhibit any toxicity on BV2 cells (Fig. 11B). Hence, we selected a concentration of 400 μM DCA for the subsequent experiments.

Hpgd, p-JAK2, JAK2, p-STAT3, and STAT3 expression levels were detected in cells using the Western blot technique. The results demonstrated that DCA reduced the expression level of Hpgd in cells and increased the ratio of p-JAK2/JAK2 and p-STAT3/STAT3 (Figs. 11C and D).

Hpgd-UP cells, an abbreviation for Hpgd overexpressing mouse microglial cells, were generated through lentiviral technology. The overexpression efficiency was assessed using RT-qPCR and Western blot, confirming the successful creation of Hpgd-UP BV2 cells (Figs. S4A–C).

The expression levels of p-JAK2, JAK2, p-STAT3, and STAT3 were detected in NC-UP cells (as a control for Hpgd-UP) and Hpgd-UP cells using the Western blot technique. The results indicated a decrease in p-JAK2/JAK2 and p-STAT3/STAT3 ratio in Hpgd-UP cells (Figs. S4D–E).

In the meantime, we generated a lentivirus that overexpresses STAT3 and employed both RT-qPCR and Western blot techniques to assess the efficiency of overexpression. The results demonstrate that STAT3-UP exhibited superior overexpression efficiency (Figs. S4F–H).

Cells from different groups were processed using DCA, and their proliferation rates were detected using the CCK-8 assay kit. The results demonstrate that the proliferation rate of NC-UP cells was higher than that of the PBS-treated group following DCA treatment. In contrast, the proliferation rate of DCA-Hpgd-UP cells was lower than that of DCA-NC-UP cells, and the proliferation rate of Hpgd-UP cells was lower than that of NC-UP cells. In the meantime, upon overexpressing STAT3, there was an increase in the proliferation rate of BV2 cells (Fig. 11E). Cell viability was assessed using MTT experiments, and similar trends were observed (Fig. 11F).

The expression level of the Iba-1 protein was analyzed using the immunofluorescence technique. The findings revealed that the DCA-NC-UP group exhibited an increase in positive cells compared to the PBS-NC-UP group. However, the DCA-Hpgd-UP group demonstrated a decrease in positive cells compared to the DCA-NC-UP group. Furthermore, the overexpression of Hpgd alone reduced the number of positive cells. However, subsequent overexpression of STAT3 increased the number of positive cells (Figs. 11G and H).

Activated microglial cells have migration and phagocytic functions. Hence, we conducted a scratch experiment to ascertain the migration capability of glial cells with varying genotypes. In BV2 cells treated with DCA, the number of migrating glial cells in the scratch area increases at different time intervals (6, 12, and 24 h) expressed as a percentage of the occupied area. However, overexpression of Hpgd leads to a decrease in migratory ability. Compared to the NC-UP group, the number of migrating cells was lower in the Hpgd-UP group. However, the introduction of STAT3-UP increased the number of migrating cells (Figs. 11I and J).

The phagocytic activity of different genotypes of microglia was assessed using pHrodo™ Green *E. coli* reagent. The results demonstrated that DCA remarkably enhanced phagocytic capability, whereas Hpgd notably diminished it. Moreover, STAT3 could counteract the effect exerted by Hpgd, as depicted in Figs. 11K and L.

To summarize, the data suggest that DCA could enhance microglial cells' activation and phagocytic capacity. This effect is achieved by suppressing the expression of Hpgd and activating the JAK2/STAT3 signaling pathway.

3.11. DCA modulates ROS production and mitochondrial autophagy in microglial cells via hpgd and JAK2/STAT3 pathways

Enhanced production of ROS within cells is a characteristic feature of activated microglia, which contributes to the release of additional pro-inflammatory factors, thereby exacerbating inflammation [32]. To further investigate this mechanism, we conducted DHE staining on BV2 cells treated with LPS to assess the production of intracellular ROS. The results demonstrated that the DCA-NC-UP group had a higher ROS level than the PBS-NC-UP group. However, the ROS levels were reduced after the overexpression of Hpgd. In addition, the Hpgd-UP group showed a decrease in ROS levels compared to the NC-UP group. However, the overexpression of STAT3 increased ROS levels (Figs. 12A and B).

Furthermore, we employed the JC-1 fluorescent dye to evaluate the mitochondrial membrane potential (MMP). Under typical mitochondrial conditions, JC-1 primarily emits red fluorescence. However, when the MMP decreases, it transitions to green fluorescence. Our experimental data demonstrates that treatment with DCA leads to a reduction in the intensity of red fluorescence. However, when Hpgd is overexpressed, there is an increase observed in the intensity of red fluorescence. However, upon re-expression of STAT3, the red fluorescence weakens (Figs. 12C and D).

To further investigate the autophagic status of cells, we employed LC3II immunofluorescence staining. Additionally, mitochondrial proteins were extracted from BV2 cells to assess the expression of autophagy markers, including LC3I, LC3II, and Beclin-1. The DCA-NC-UP group showed a decrease in autophagy compared to the PBS-NC-UP group. However, overexpression of Hpgd led to an enhancement of autophagy. The Hpgd-UP group exhibited a notable augmentation in autophagy compared to the NC-UP group. Nonetheless, there was a decline in autophagy following the re-expression of STAT3 (Figs. 12E–H).

We conducted co-immunostaining of p62, which is involved in recognizing damaged proteins and the autophagy process, and

Fig. 11. Investigating the effect of dichloroacetate (DCA) on hydroxyprostaglandin dehydrogenase (Hpgd) expression in microglial cells and its activation on the Janus kinase 2 (JAK2)/signal transducer and activator of transcription 3 (STAT3) pathway. (A) Real-time quantitative polymerase chain reaction (RT-qPCR) to measure the expression levels of pro-inflammatory cytokines tumor necrosis factor alpha (TNF-α), interleukin (IL)-1β, IL-6, and IL-4 in BV2 cells. (B) Lactate dehydrogenase (LDH) release in BV2 cells at different concentrations of DCA. (C, D) Analysis of the expression levels of Hpgd, p-JAK2, JAK2, p-STAT3, and STAT3 in BV2 cells following DCA treatment (C) and the statistical chart (D). (E) Assessment of cell proliferation using Cell Counting Kit-8 (CCK-8) assay. (F) Measurement of cell viability using an 3-(4,5-dimethylthiazol-2-yl)-2,5-diphenyltetrazolium bromide (MTT) assay. (G, H) Immunofluorescence staining to determine the expression level of Iba-1 in BV2 cells (G) and the statistical chart of positive cells (H). (I, J) Imaging BV2 cells migrating to the scratch area at different time points (6, 12, and 24 h) (H) and calculation of the percentage of migrated cells performed using ImageJ software (J). (K, L) Observation (K) and quantification (L) of pHrodo™ Green *Escherichia coli* (*E. coli*) particles using fluorescence microscopy. All cell experiments were repeated three times, and the values are presented as mean ± standard deviation (SD). In Figs. 11A and B, the asterisks (*, **, and ***) indicates a difference compared to DCA (0 μM), $^*P < 0.05$, $^{**}P < 0.01$, and $^{***}P < 0.001$. mRNA: messenger RNA; PBS: phosphate-buffered saline; DAPI: 4',6-diamidino-2-phenylindole; Iba-1: ionized calcium-binding adapter molecule 1; FITC: fluorescein isothiocyanate.

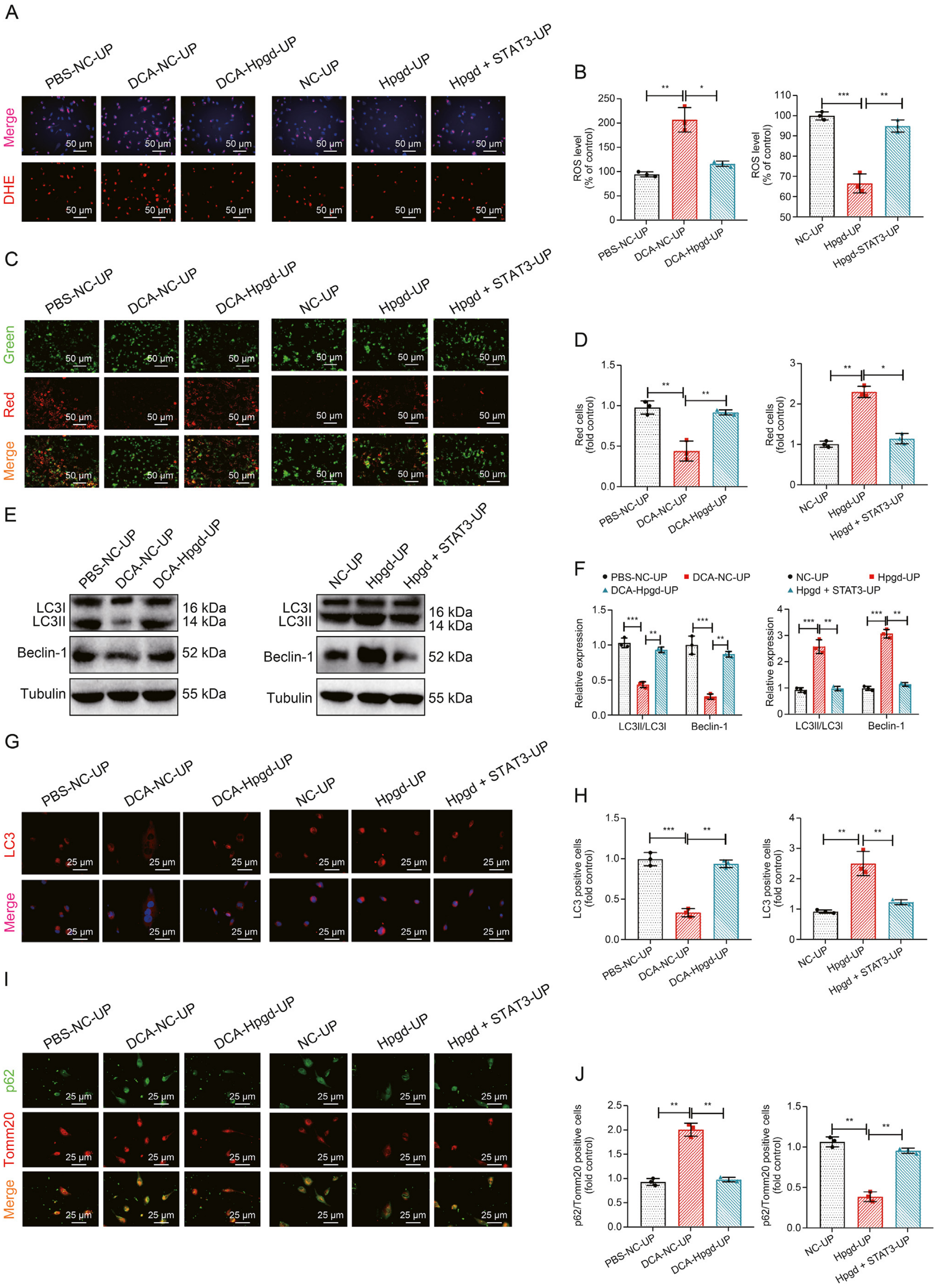
A
PBS-NC-UP
DCA-NC-UP
DCA-Hpgd-UP
NC-UP
Hpgd-UP
Hpgd + STAT3-UP
Merge
DHE
50 μm
B
ROS level (% of control)
250
200
150
100
50
0
**
*
PBS-NC-UP
DCA-NC-UP
DCA-Hpgd-UP
110
100
90
80
70
60
50
***
**
NC-UP
Hpgd-UP
Hpgd-STAT3-UP
C
Green
Red
Merge
D
Red cells (fold control)
1.5
1.0
0.5
0.0
3
2
1
0
E
LC3I
LC3II
Beclin-1
Tubulin
16 kDa
14 kDa
52 kDa
55 kDa
F
● PBS-NC-UP ■ DCA-NC-UP ▲ DCA-Hpgd-UP
● NC-UP ■ Hpgd-UP ▲ Hpgd + STAT3-UP
Relative expression
LC3II/LC3I
Beclin-1
4
G
LC3
25 μm
H
LC3 positive cells (fold control)
I
p62
Tomm20
J
p62/Tomm20 positive cells (fold control)
2.5
2.0

Tomm20, a protein found in the outer mitochondrial membrane, to further investigate changes in mitophagy. The data indicates that treatment with DCA leads to an increase in aggregates containing p62 that co-localize with mitochondria, suggesting the inhibition of mitophagy. However, overexpression of Hpgd can significantly reduce the colocalization of p62 with mitochondria, but upon re-overexpression of STAT3, the colocalization substantially increases (Figs. 12I and J).

DCA promotes the generation of ROS and inhibits mitochondrial autophagy, whereas Hpgd has the opposite effect by inhibiting ROS generation and promoting mitochondrial autophagy.

3.12. DCA-induced microglial inflammation impacts neuronal viability and functionality via the HpgdJAK2/STAT3 signaling pathway

Interactions between neurons and glial cells are crucial in maintaining the neuroimmune system [33]. DCA could promote the activation and proliferation of microglial cells and inhibit the mitochondrial autophagy of these cells. Analysis of scRNA-seq data revealed an increase in the number of neurons following FMT treatment. Next, we examined the effects of microglial cell inflammation on neurons.

The mouse hippocampal neuron cell line HT22 was labeled with GFP and then co-cultured with BV2 cells that were treated differently. We performed real-time longitudinal tracking of HT22 cells using a high-resolution microscope system. By combining flow cytometry analysis, our findings revealed that DCA greatly augmented HT22 cell apoptosis, whereas overexpression of Hpgd considerably inhibited this apoptotic phenomenon. As neurons are incapable of proliferation, the sole overexpression of Hpgd did not yield any differences. Furthermore, upon re-expression of STAT3, there was an increase in the number of apoptotic cells (Figs. 13A–D).

Simultaneously, we employed the patch clamp technique to record the action potentials of neurons. The analysis results indicate that the discharge frequency of neurons' action potentials decreases under DCA-NC-UP processing. Furthermore, the expression of Hpgd leads to restoring the discharge frequency. Compared to the NC-UP group, the Hpgd-UP group displayed an increase in the action potential frequency of HT22 cells. However, when STAT3 is re-overexpressed and the frequency decreases, as shown in Figs. 13E and F.

Our research uncovered the pivotal role of DCA in regulating the inflammatory response of microglia and mitophagy. Moreover, we elucidated its influence on neuronal apoptosis and electrical abnormalities via the Hpgd/JAK2/STAT3 signaling pathway, offering a novel theoretical foundation and potential therapeutic targets for neuroimmune regulation.

4. Discussion

This study investigates the association between NAFLD and cognitive dysfunction using a comprehensive approach combining 16S rRNA sequencing and single-cell transcriptome sequencing [34]. In recent years, NAFLD has been acknowledged as a systemic metabolic disorder, expanding beyond its initial classification as solely a liver-related condition [35,36]. This study offers additional evidence for this perspective and highlights the connection between gut microbiota and brain function. Despite investigating the gut-brain axis mechanism in several diseases, its study in the context of NAFLD still lacks depth [2,37,38].

Our findings reveal a substantial dissimilarity in gut microbiota composition between NAFLD patients and healthy individuals, specifically showcasing an elevated abundance of *Bacteroides* [39]. This finding aligns with previous studies demonstrating that an imbalance in the gut microbiota could impact liver function and metabolism [40,41]. The elevation of *Bacteroides* levels could be linked to the progression and pathophysiology of NAFLD.

In addition to alterations in the microbiota, there was a notable elevation in the *Bacteroides*-associated metabolite DCA in mice with NAFLD. This finding emphasizes the significance of the metabolic interactions between microbes and hosts, indicating that DCA could be a crucial mediator in the liver-gut-brain axis. Previous studies have also acknowledged the involvement of DCA in various diseases. However, the specific mechanisms of DCA in the context of NAFLD still require further clarification [42].

Our experimental findings demonstrate that DCA effectively inhibits the expression of Hpgd and activates the JAK2/STAT3 signaling pathway in glial cells. This process could result in neuronal apoptosis and reduced action potentials. These findings offer possible molecular mechanisms for brain dysfunction related to NAFLD, which is in contrast to previous studies that primarily focused on the effects of DCA on the liver rather than the central nervous system [5].

Following FMT treatment, we observed improved liver and brain function in NAFLD mice. This study offers novel insights into managing NAFLD and its associated complications. FMT has been documented as a therapeutic approach for various diseases. However, it remains in the exploratory phase in the context of NAFLD. Thus, this discovery holds substantial innovative potential.

This study offers comprehensive insights into the influence of NAFLD on brain function and cognition via the liver-gut-brain axis. Additionally, it explores the potential of improving these effects through FMT. DCA has been shown to potentially play a vital role as a metabolic molecule in facilitating communication between the liver and the brain. Additionally, it affects the activation of microglial cells and mitochondrial autophagy (Fig. 14).

The study encompasses several important fields, such as metabolic diseases, immunology, neuroscience, and molecular biology. Numerous novel disease pathways and potential therapeutic targets have been unveiled through a comprehensive analysis of DCA's mechanism of action in NAFLD treatment and the regulatory role of Hpgd in microglial cells.

Although our study has revealed the impact of NAFLD on brain function and cognition, as well as potential therapeutic mechanisms, it is important to acknowledge the limitations present in this research that require deeper exploration and resolution in future studies. Firstly, our study only conducted metabolomic analysis on fecal samples from NAFLD patients. The connections between the liver, intestines, and brain are achieved through the circulation of blood. Conducting serum, liver, or brain tissue metabolomic analysis facilitated a better understanding of the pathogenic mechanisms of NAFLD, and this will be a focus of our future research.

Fig. 12. Investigation of mitochondrial dysfunction and microglial activation mechanisms. (A, B) Measurement of reactive oxygen species (ROS) accumulation in cells by dihydroethidium (DHE) assay and monitoring by fluorescence microscopy (A) and statistical chart (B). (C, D) Detection of mitochondrial membrane potential (MMP) in BV2 cells using 5,5',6,6'-tetrachloro-1,1',3,3'-tetraethylbenzimidazolylcarbocyanine iodide (JC-1) staining (C) and statistical chart (D). (E, F) Performance of Western blot to measure the expression levels of autophagy markers in BV2 cells (E) and statistical chart (F). (G, H) Utilization of immunofluorescence staining to determine the expression level of microtubule-associated protein 1a/1b-light chain 3 (LC3) in BV2 cells (G) and statistical chart (H). (I, J) Analysis of subcellular distribution of p62 and mitochondria (translocase of outer mitochondrial membrane 20 (Tomm20)) in BV2 cells by confocal microscopy (I) and statistical chart of positive cells (J). All cell experiments were repeated three times, and the values are presented as mean ± standard deviation (SD). $^{*}P < 0.05$, $^{**}P < 0.01$, and $^{***}P < 0.001$. PBS: phosphate-buffered saline; DCA: dichloroacetate; Hpgd: hydroxyprostaglandin dehydrogenase.

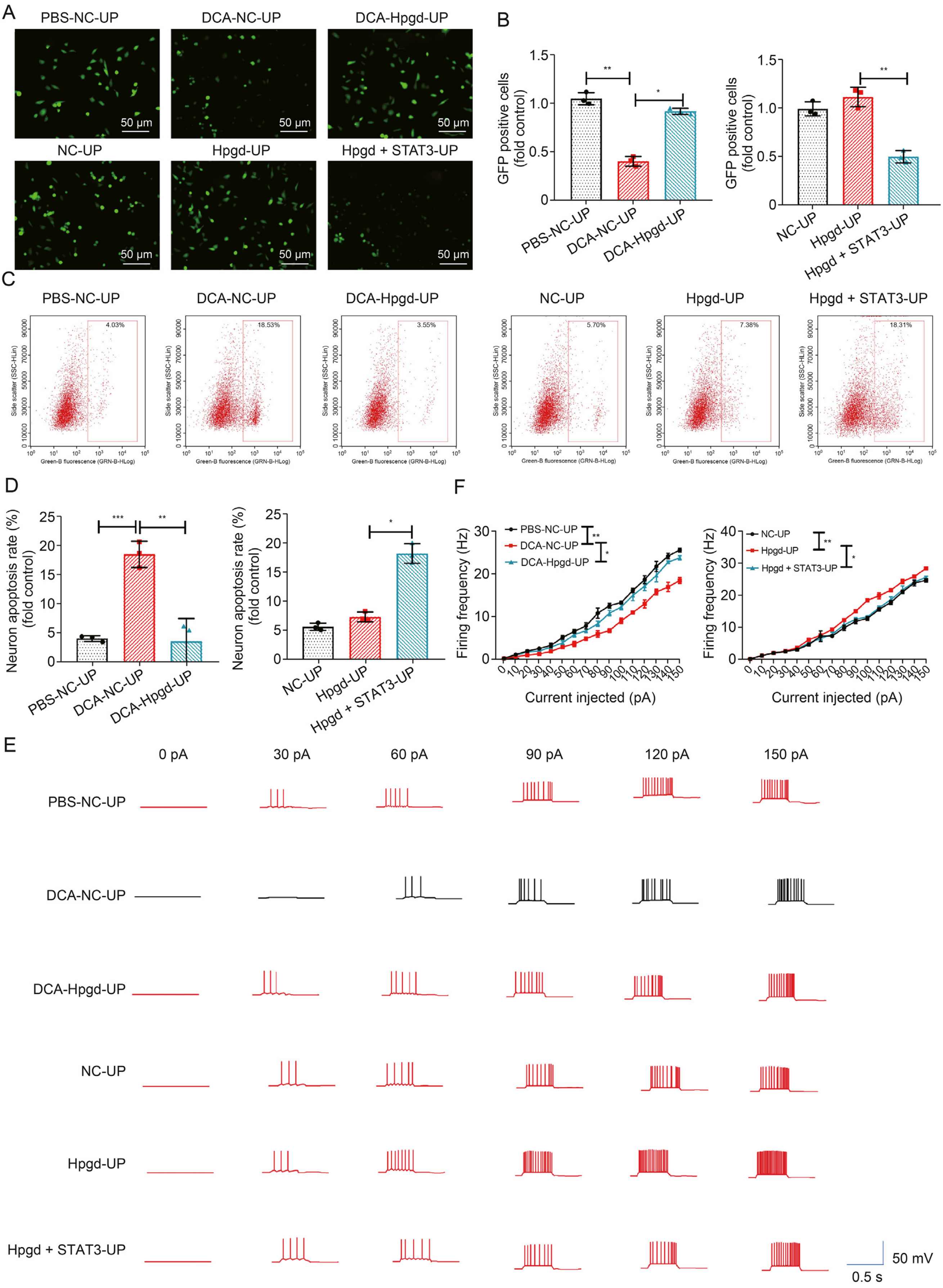
A
PBS-NC-UP
DCA-NC-UP
DCA-Hpgd-UP
NC-UP
Hpgd-UP
Hpgd + STAT3-UP
50 μm
B
GFP positive cells (fold control)
1.5
1.0
0.5
0
**
*
PBS-NC-UP
DCA-NC-UP
DCA-Hpgd-UP
NC-UP
Hpgd-UP
Hpgd + STAT3-UP
C
PBS-NC-UP
DCA-NC-UP
DCA-Hpgd-UP
NC-UP
Hpgd-UP
Hpgd + STAT3-UP
4.03%
18.53%
3.55%
5.70%
7.38%
18.31%
Side scatter (SSC-HLin)
Green-B fluorescence (GRN-B-HLog)
D
Neuron apoptosis rate (%) (fold control)
25
20
15
10
5
0
***
**
*
PBS-NC-UP
DCA-NC-UP
DCA-Hpgd-UP
NC-UP
Hpgd-UP
Hpgd + STAT3-UP
F
Firing frequency (Hz)
PBS-NC-UP
DCA-NC-UP
DCA-Hpgd-UP
NC-UP
Hpgd-UP
Hpgd + STAT3-UP
Current injected (pA)
E
0 pA
30 pA
60 pA
90 pA
120 pA
150 pA
PBS-NC-UP
DCA-NC-UP
DCA-Hpgd-UP
NC-UP
Hpgd-UP
Hpgd + STAT3-UP
50 mV
0.5 s

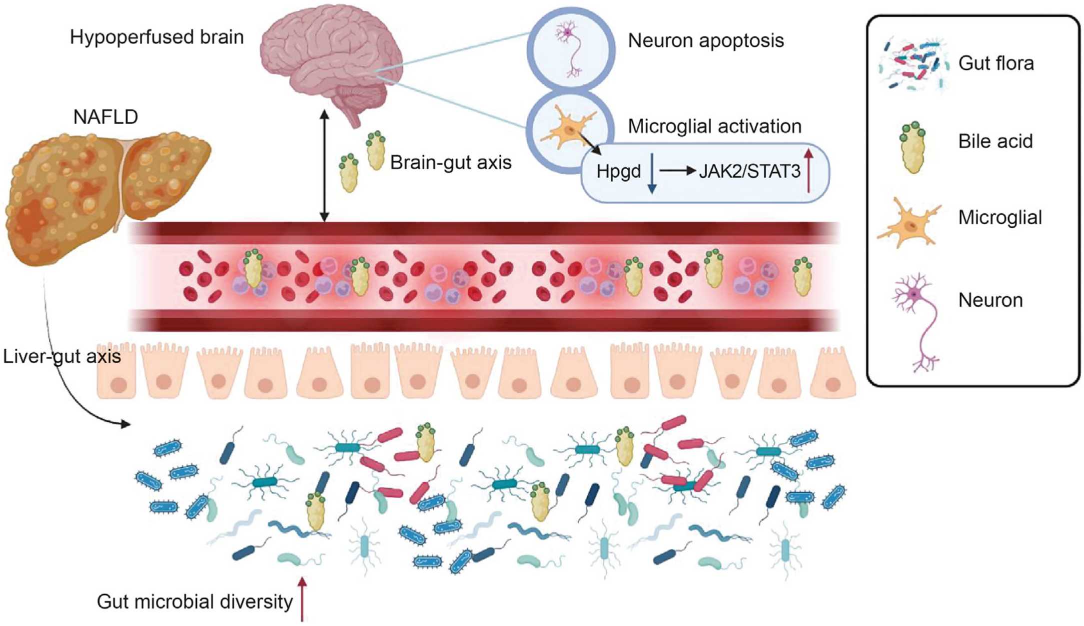

Fig. 14. Molecular mechanism of liver-gut-brain axis in non-alcoholic fatty liver disease (NAFLD)-induced brain dysfunction. Hpgd: hydroxyprostaglandin dehydrogenase; JAK2: Janus kinase 2; STAT3: signal transducer and activator of transcription 3.

Additionally, our study primarily relied on mouse models; therefore, further clinical research is necessary to validate our findings before applying them to human patients.

Furthermore, although our study delved into detailed molecular and cellular mechanisms, a more in-depth understanding of the precise mechanisms of action of DCA in the liver-intestine-brain cycle is still needed. For example, does DCA act directly on Hpgd, or does it inhibit Hpgd expression through the nuclear transcription factor κB (NF-κB) [43]? Moreover, are there other regulatory elements involved in the inhibition of JAK2/STAT3 by Hpgd, such as prostaglandins [44]? The specific pathway through which JAK2/STAT3 activates microglial cells remains unstudied. Whether it is through the inhibition of microglial cell apoptosis by Bcl-extra large (Bcl-XL) [45], enhancement of microglial cell proliferation by Cyclin D1 [46], or other unexplored pathways will be the focus of our research. Future studies are needed to uncover how DCA crosses the blood-brain barrier and its interactions with other signaling molecules in the brain. Apart from DCA, the two types of secondary bile acids observed in our study will also be areas of further investigation.

In summary, our study not only enhances understanding of NAFLD and neuroimmune system diseases but also provides valuable insights for future therapeutic strategies and mechanism research. These findings hold promise for the development of new treatment methods, drugs, and therapeutic targets to improve the quality of life for patients suffering from metabolic and neurological diseases. Further research will help unlock the full potential of these fields, providing new directions and hope for future medical advancements.

5. Conclusions

In conclusion, this study has not only improved our understanding of NAFLD and neuroimmune system disorders but also offered valuable insights for future therapeutic interventions and mechanistic investigations. These findings are anticipated to greatly advance novel treatment approaches, medications, and therapeutic targets, enhancing the overall quality of life for patients suffering from metabolic and neurological disorders. Further research will assist in unleashing the complete potential of these fields, offering new pathways and optimism for future medical advancements.

Ethical statement

This study was conducted in strict accordance with the ethical guidelines for animal research and was approved by the Institutional Animal Care and Use Committee of China Medical University, China. The study was assigned the animal ethics approval number CMU2022278.

CRediT authorship contribution statement

Jingting Zhang: Writing – review & editing, Writing – original draft, Software, Resources, Methodology, Investigation, Formal analysis, Data curation, Conceptualization. **Keyan Chen:** Writing – review & editing, Writing – original draft, Resources, Methodology, Investigation, Data curation, Conceptualization. **Fu Chen:** Writing – review & editing, Validation, Supervision, Resources, Project administration, Formal analysis, Data curation, Conceptualization.

Declaration of competing interest

The author declares no conflict of interest.

Fig. 13. Investigating the impact of dichloroacetate (DCA) on microglial cell function and its effect on neuronal physiological activity. (A, B) Fluorescence images of green fluorescent protein (GFP)-labeled HT22 cells (A) and the statistical chart of GFP-positive cells (B). (C, D) Flow cytometry was used to detect apoptosis in HT22 cells (C) and the statistical chart of apoptotic cells (D). (E, F) Representative traces of action potentials of neurons at different current levels (E) and the firing frequency (F) of action potentials in neurons. The injected current range was 0 to 150 pA. All cell experiments were repeated three times, and the values are presented as mean ± standard deviation (SD). $^{*}P < 0.05$, $^{**}P < 0.01$, and $^{***}P < 0.001$. PBS: phosphate-buffered saline.

Acknowledgments

This work was supported by National Natural Science Foundation of China (Grant No.: 82200971), China Postdoctoral Science Foundation funded project (Grant No.: 2023MD744267), and Project of Liaoning Provincial Department of Science and Technology, China (Grant Nos.: 2023JH2/20200120 and 2022-MS-180).

Appendix A. Supplementary data

Supplementary data to this article can be found online at https://doi.org/10.1016/j.jpha.2024.101077.

References

[1] A.G. Singal, P. Lampertico, P. Nahon, Epidemiology and surveillance for hepatocellular carcinoma: New trends, J. Hepatol. 72 (2020) 250–261.

[2] E.E. Powell, V.W. Wong, M. Rinella, Non-alcoholic fatty liver disease, Lancet 397 (2021) 2212–2224.

[3] D. Yardeni, R. Toledano, V. Novack, et al., The association of alanine aminotransferase levels with myocardial perfusion imaging and cardiovascular morbidity, J. Cardiovasc. Pharmacol. Ther. 27 (2022), 10742484221074585.

[4] N. Stefan, K. Cusi, A global view of the interplay between non-alcoholic fatty liver disease and diabetes, Lancet Diabetes Endocrinol. 10 (2022) 284–296.

[5] A. Hadjihambi, C. Konstantinou, J. Klohs, et al., Partial MCT1 invalidation protects against diet-induced non-alcoholic fatty liver disease and the associated brain dysfunction, J. Hepatol. 78 (2023) 180–190.

[6] B. Filipovic, S. Lukic, D. Mijac, et al., The new therapeutic approaches in the treatment of non-alcoholic fatty liver disease, Int. J. Mol. Sci. 22 (2021), 13219.

[7] A. Garcia-Romeu, S. Darcy, H. Jackson, et al., Psychedelics as novel therapeutics in Alzheimer's disease: rationale and potential mechanisms, Curr. Top. Behav. Neurosci. 56 (2022) 287–317.

[8] J. Chen, L. Vitetta, Gut microbiota metabolites in NAFLD pathogenesis and therapeutic implications, Int. J. Mol. Sci. 21 (2020), 5214.

[9] H. Tilg, T.E. Adolph, M. Dudek, et al., Non-alcoholic fatty liver disease: The interplay between metabolism, microbes and immunity, Nat. Metab. 3 (2021) 1596–1607.

[10] P.D. Cani, C. Depommier, M. Derrien, et al., *Akkermansia muciniphila*: Paradigm for next-generation beneficial microorganisms, Nat. Rev. Gastroenterol. Hepatol. 19 (2022) 625–637.

[11] Q. Hu, W. Zhang, Z. Wu, et al., Baicalin and the liver-gut system: Pharmacological bases explaining its therapeutic effects, Pharmacol. Res. 165 (2021), 105444.

[12] X. Zhang, O.O. Coker, E.S. Chu, et al., Dietary cholesterol drives fatty liver-associated liver cancer by modulating gut microbiota and metabolites, Gut 70 (2021) 761–774.

[13] Z. Mészáros, P. Nekvasilová, P. Bojarová, et al., Advanced glycosidases as ingenious biosynthetic instruments, Biotechnol. Adv. 49 (2021), 107733.

[14] P. Tavakoli, U. Vollmer-Conna, D. Hadzi-Pavlovic, et al., A review of inflammatory bowel disease: a model of microbial, immune and neuropsychological integration, Public Health Rev 42 (2021), 1603990.

[15] Y. Pu, Y. Tan, Y. Qu, et al., A role of the subdiaphragmatic vagus nerve in depression-like phenotypes in mice after fecal microbiota transplantation from Chrna7 knock-out mice with depression-like phenotypes, Brain Behav. Immun. 94 (2021) 318–326.

[16] T. Tsuchida, Y.A. Lee, N. Fujiwara, et al., A simple diet- and chemical-induced murine NASH model with rapid progression of steatohepatitis, fibrosis and liver cancer, J. Hepatol. 69 (2018) 385–395.

[17] W. Xiao, J. Su, X. Gao, et al., The microbiota-gut-brain axis participates in chronic cerebral hypoperfusion by disrupting the metabolism of short-chain fatty acids, Microbiome 10 (2022), 62.

[18] Z. Liu, X. Dai, H. Zhang, et al., Gut microbiota mediates intermittent-fasting alleviation of diabetes-induced cognitive impairment, Nat. Commun. 11 (2020), 855.

[19] L. Chen, X. Zhang, Q. Zhang, et al., A necroptosis related prognostic model of pancreatic cancer based on single cell sequencing analysis and transcriptome analysis, Front. Immunol. 13 (2022), 1022420.

[20] S. Feng, L. Gao, D. Zhang, et al., MiR-93 regulates vascular smooth muscle cell proliferation, and neointimal formation through targeting Mfn2, Int. J. Biol. Sci. 15 (2019) 2615–2626.

[21] A. Shah, L. Xia, H. Goldberg, et al., Thioredoxin-interacting protein mediates high glucose-induced reactive oxygen species generation by mitochondria and the NADPH oxidase, Nox4, in mesangial cells, J. Biol. Chem. 288 (2013) 6835–6848.

[22] C. Wu, Z. Shen, Y. Lu, et al., p53 promotes ferroptosis in macrophages treated with Fe_3O_4 nanoparticles, ACS Appl. Mater. Interfaces 14 (2022) 42791–42803.

[23] A.J. Sanyal, M.L. Van Natta, J. Clark, et al., Prospective study of outcomes in adults with nonalcoholic fatty liver disease, N. Engl. J. Med. 385 (2021) 1559–1569.

[24] N. Jiao, S.S. Baker, A. Chapa-Rodriguez, et al., Suppressed hepatic bile acid signalling despite elevated production of primary and secondary bile acids in NAFLD, Gut 67 (2018) 1881–1891.

[25] S. Lechner, M. Yee, B.N. Limketkai, et al., Fecal microbiota transplantation for chronic liver diseases: Current understanding and future direction, Dig. Dis. Sci. 65 (2020) 897–905.

[26] S. MahmoudianDehkordi, M. Arnold, K. Nho, et al., Altered bile acid profile associates with cognitive impairment in Alzheimer's disease – An emerging role for gut microbiome, Alzheimers Dement. 15 (2019) 76–92.

[27] J.M. Rorabaugh, T. Chalermpalanupap, C.A. Botz-Zapp, et al., Chemogenetic locus coeruleus activation restores reversal learning in a rat model of Alzheimer's disease, Brain 140 (2017) 3023–3038.

[28] X. Pan, C.T. Elliott, B. McGuinness, et al., Metabolomic profiling of bile acids in clinical and experimental samples of Alzheimer's disease, Metabolites 7 (2017), 28.

[29] S. Yao, J. Xu, K. Zhao, et al., Down-regulation of HPGD by miR-146b-3p promotes cervical cancer cell proliferation, migration and anchorage-independent growth through activation of STAT3 and AKT pathways, Cell Death Dis. 9 (2018), 1055.

[30] H. Zhu, Z. Jian, Y. Zhong, et al., Janus kinase inhibition ameliorates ischemic stroke injury and neuroinflammation through reducing NLRP3 inflammasome activation via JAK2/STAT3 pathway inhibition, Front. Immunol. 12 (2021), 714943.

[31] X. Han, T. Xu, Q. Fang, et al., Quercetin hinders microglial activation to alleviate neurotoxicity via the interplay between NLRP3 inflammasome and mitophagy, Redox Biol. 44 (2021), 102010.

[32] H. Liu, Y. Han, T. Wang, et al., Targeting microglia for therapy of Parkinson's disease by using biomimetic ultrasmall nanoparticles, J. Am. Chem. Soc. 142 (2020) 21730–21742.

[33] J.T. Rogers, J.M. Morganti, A.D. Bachstetter, et al., CX3CR1 deficiency leads to impairment of hippocampal cognitive function and synaptic plasticity, J. Neurosci. 31 (2011) 16241–16250.

[34] T. Li, X. Lin, B. Shen, et al., *Akkermansia muciniphila* suppressing nonalcoholic steatohepatitis associated tumorigenesis through CXCR6$^+$ natural killer T cells, Front. Immunol. 13 (2022), 1047570.

[35] X. Qi, J. Lai, Exosomal microRNAs and progression of nonalcoholic Steatohepatitis (NASH), Int. J. Mol. Sci. 23 (2022), 13501.

[36] H. El Hadi, A. Di Vincenzo, R. Vettor, et al., Cardio-metabolic disorders in non-alcoholic fatty liver disease, Int. J. Mol. Sci. 20 (2019), 2215.

[37] J.F. Cryan, K.J. O'Riordan, C.S.M. Cowan, et al., The microbiota-gut-brain axis, Physiol Rev. 99 (2019) 1877–2013.

[38] E.A. Mayer, K. Nance, S. Chen, The gut-brain axis, Annu. Rev. Med. 73 (2022) 439–453.

[39] S. Preethy, N. Ikewaki, G.A. Levy, et al., Two unique biological response-modifier glucans beneficially regulating gut microbiota and faecal metabolome in a non-alcoholic steatohepatitis animal model, with potential applications in human health and disease, BMJ Open Gastroenterol. 9 (2022), e000985.

[40] S.L. Collins, J.G. Stine, J.E. Bisanz, et al., Bile acids and the gut microbiota: Metabolic interactions and impacts on disease, Nat. Rev. Microbiol. 21 (2023) 236–247.

[41] L. Wang, Z.-M. Cao, L.-L. Zhang, et al., The role of gut microbiota in some liver diseases: From an immunological perspective, Front. Immunol. 13 (2022), 923599.

[42] N. Farooqui, A. Elhence, Shalimar, A current understanding of bile acids in chronic liver disease, J. Clin. Exp. Hepatol. 12 (2022) 155–173.

[43] J.-Y. Li, J.-P. Chen, Y.-L. Qian, et al., Follicular fluid progesterone downregulated HPGD and COX2 in granulosa cells via suppressing NF-κB in endometriosis, Biol. Reprod. 108 (2023) 791–801.

[44] L. Shu, X. Li, Z. Liu, et al., Bile exosomal miR-182/183-5p increases cholangiocarcinoma stemness and progression by targeting HPGD and increasing PGE2 generation, Hepatology 79 (2024) 307–322.

[45] M.Y. Kuo, W.C. Dai, J.-L. Chang, et al., Fucoxanthin induces human melanoma cytotoxicity by thwarting the JAK2/STAT3/BCL-xL signaling axis, Environ Toxicol. 39 (2024) 3356–3366.

[46] X. Chen, H. Chen, Y. He, et al., Proteomics-guided study on buyang huanwu decoction for its neuroprotective and neurogenic mechanisms for transient ischemic stroke: Involvements of EGFR/PI3K/Akt/bad/14-3-3 and Jak2/Stat3/cyclin D1 signaling cascades, Mol. Neurobiol. 57 (2020) 4305–4321.